Lawrence Berkeley National Laboratory
Recent Work

Title
ELECTRON MICROSCOPY STUDIES OF ION IMPLANTED SILICON

Permalink
https://escholarship.org/uc/item/10t9s3s1

Author
Seshan, Krishna.

Publication Date
1975-11-01

eScholarship.org Powered by the California Digital Library
University of California

LBL-2728
c.2

ELECTRON MICROSCOPY STUDIES OF ION IMPLANTED SILICON

Krishna Seshan
(Ph. D. thesis)

November 1975

Prepared for the U. S. Energy Research and Development Administration under Contract W-7405-ENG-48

TWO-WEEK LOAN COPY

This is a Library Circulating Copy which may be borrowed for two weeks. For a personal retention copy, call Tech. Info. Division, ~~Ext. 5545~~

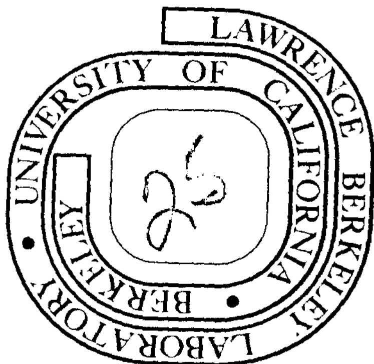

LBL-2728
c.2

DISCLAIMER

This document was prepared as an account of work sponsored by the United States Government. While this document is believed to contain correct information, neither the United States Government nor any agency thereof, nor the Regents of the University of California, nor any of their employees, makes any warranty, express or implied, or assumes any legal responsibility for the accuracy, completeness, or usefulness of any information, apparatus, product, or process disclosed, or represents that its use would not infringe privately owned rights. Reference herein to any specific commercial product, process, or service by its trade name, trademark, manufacturer, or otherwise, does not necessarily constitute or imply its endorsement, recommendation, or favoring by the United States Government or any agency thereof, or the Regents of the University of California. The views and opinions of authors expressed herein do not necessarily state or reflect those of the United States Government or any agency thereof or the Regents of the University of California.

To Amma, Appa and Kamala . . .

"The rare moment, is not the moment when there is something worth looking at, but the moment when we are capable of seeing." Joseph Krutch

Preface

Scientific activity must simplify and unify if the present escalation of "result producing" is not to totally obscure pertinent problems. Often during the period of this study I have wondered which I was doing. As it turns out a slight amount of simplification has been achieved, but perhaps not nearly enough.

For the rest, I am left puzzled by the philosophy of research. The clear connection between hypothesis, experiment and result was only seen post facto. However, this was a rich experience in looking, and looking carefully. More than anyone else, perhaps it is the electron microscopist who should report not merely what is seen but try to observe, understand and present a unifying pattern in what is seen.

CONTENTS

Preface

Abstract vii

Introduction 1

Chapter I. Summary of the Results of Previous Investigators.

Topics Investigated 4

Chapter II. Specimen Preparation 14

Chapter III. Optimum Imaging Condition and Image Complexities . . 21

Chapter IV. Characterization of the Defects 40

Chapter V. A Model for the Presence of Interstitial Defects . . . 74

ELECTRON MICROSCOPY STUDIES OF ION IMPLANTED SILICON

Krishna Seshan

Inorganic Materials Research Division, Lawrence Berkeley Laboratory and
Department of Materials Science and Engineering, College of Engineering;
University of California, Berkeley, California 94720

Abstract

"Accidential and fortutious concurrance of atoms". A. J. Temple

The nature of defects resulting from the rapid implantation of accelerated phosphorous ions into silicon and a model of how they form are reported. This involved an electron microscope study of the crystallographic defects (in the 300Å size range in concentration of $10^{15}/cm^3$) that form upon annealing. The annealing step, where the bombarded silicon is heated to relatively low temperatures (800°C), repairs the bombardment damage and in addition restors the implanted atoms to electrically active sites.

Studies using high (650 kV) voltage as well as standard (100 kV) electron microscopes showed that the images formed by these crystallographic defects are complex and that nonconventional imaging techniques are required for their characterization. Such studies revealed the optimum imaging conditions for the imaging of these defects and showed that the images of these small defects (about 300Å or 3×10^{-6} cm) are sensitive to various parameters, such as the foil thickness, their position in the foil and the diffracting conditions.

Several nonconventional techniques were then used to characterize the defects. They were found to be mostly interstitial hexagonal Frank loops lying on the four {111} planes and a few perfect interstitial loops; these loops occurred in concentrations of about $10^{16}/cm^3$. In addition,

"rod like" linear defects that are shown to be interstitial are also found in concentrations of $10^{13}/cm^3$. By varying the prior dopants in silicon it was found that the linear defects require boron for their formation. The loops show electron diffraction contrast effects which have been interpreted as arising from some of the dopant atoms being segregated to the interior of the loops.

A model is proposed to account for the interstitial defects. Attention is drawn to the fact that the number of point defects that make up the defects is of the same order as the number of implanted ions. The model predicts that only interstitial loops ought to be observed in agreement with several recent investigations.

Dislocation models of the loops are examined and it is shown that phosphorous ions could segregate to the Frank loops, changing their displacement vectors to a/x[111]. $(x > 3)$ thus explaining the contrast effects observed. It would also explain the relative electrical inactivity of P^+ ions implanted under the conditions of this experiment--a fact that cannot be explained by present theory.

"Make for yourself a definition or description of the thing which is presented to you so as to see distinctly what kind of a thing it is in its substance, in its nudity, in its entirety and tell yourself its proper name and the names of the things of which it has been compounded and into which it will be resolved." Marcus Aurelius

INTRODUCTION

Ion implantation has currently become a popular method for doping semiconductors, thereby, introducing electrically active species in small quantities, in the parts per million range, to beneficially alter electrical properties. This technique is faster and permits greater control of dose and depth of the dopant species than the conventional diffusion doping technique. The depth is determined by the accelerating voltage (100 keV in the study) and the dose by the fluence used (3×10^{14} ions/cm^2). This rapid implantation leads to severe damage of the implanted substrate which in this study was (111) oriented silicon. The implantation damage is largely removed and a majority of the dopants are restored to electrically active sites by heating the substrate to relatively low temperatures between 500 to 800°C for about 15 min to 1/2 hr. A debris of small crystallographic defects in the 100 to 300Å size range, in high densities of about 10^{16} defects per cubic centimeter results from this annealing treatment. An investigation into the nature of these defects and the development of a model to explain how they form and affect the electrical activity of the dopants were the prime objectives of the study.

In the first chapter it is shown that for the dose used in this study, isolated and buried damage clusters are expected. Point defect studies showing that annealing in the 100 to 400° centigrade range is accompanied by the disappearance of vacancies and vacancy complexes are presented.

From this it is tempting to draw the incorrect conclusion that vacancy type defects are expected to form. The several electron microscopic studies of the defects formed on annealing and their contradictory descriptions are then pointed out. Lastly, the specific questions that this study undertook to resolve are set out.

In the second chapter, the implantation procedure and the techniques used to anneal the samples and prepare thin foils for electron microscopy are described.

In the third chapter experiments to determine the best imaging conditions for the defects are described. Studies with the 650 kV Berkeley high voltage electron microscope showed that good images were obtained with second and third order reflections excited for g = 220 and g = 111 respectively. However, it was found that at high voltages the strong effects of several systematic beams introduce complexities in image behavior. Images of the defects disappeared anamalously in both bright and dark fields. From this study it was evident that the best resolution was obtained at 100 kV using nonconventional electron microscopy: weak-beam, the symmetric weak-beam beam bright

field and systematic bright field techniques.

The fourth chapter describes the results of applying such technqiues to characterize the defects. For doses where a continuously damaged layer is not formed, the defects that develop upon annealing are shown to be interstitial Frank loops on the four {111} planes. In addition, there are a few unfaulted loops as well as rod-like defects. The rods appear to be interstitial in nature and require boron for their formation. Stereo microscopic data shows that the horizontal rods lie at the same depth as the loops whereas the inclined rods start at the level of the loops and extend upwards towards the implanted surface. They anneal from the ends in the temperature range of 700 to 750° centigrade.

In the fifth chapter a model accounting for the observed defects is presented. Contrast effects and the sensitivity of defect morphology to trace impurities are taken as evidence for interaction between the dopants and the defects. This is put forth as a feasible explanation for the poor electrical activity of foils implanted to this dose as well as the widely differing accounts of defect character in the literature. A four stage sequence involving the break up conversion and growth of interstitial clusters is proposed to account for the observed interstitial defects.

CHAPTER I.
SUMMARY OF THE RESULTS OF PREVIOUS INVESTIGATORS
TOPICS INVESTIGATED

1.1. Introduction 5

1.2. Summary of Previous Investigations 7

1.2.1. Type of Damage Expected. Critical Dose Calculations . 7

1.2.2. Present Evidence of Damage Annealing 9

1.2.3. Electron Microscope Studies 10

1.3. Discussion. Topics Investigated 12

"The Science appeared to me an elaborate diabolical invention for mystifying what was clear, and confounding what was intelligible."

N. Sinclair

1.1. Introduction

The field of ion implantation has proved to be a rich source of information in areas of radiation damage and defect studies in silicon. The incoming energenic ion deposits its energy in the target first by ionization and then by nuclear collisions. Radiation damage theory has been successful in calculating the ion range distribution and describing the type of damage caused (Gibbons, 1971). Electron paramagnetic resonance (EPR) (Watkins, 1965) and infrared absorption (IR) studies havebeen especially successful in elucidating the nature of the point defects produced by the collisions and their electronic nature, some of the complexes they form and their range of stabilities have been carefully mapped (Cheng et al., 1966).

There are, however, several limitations to such studies since the defects have to be electrically or electronically active in order to be detected by EPR or IR spectroscopy. Of special relevance is the reported interstitial problem: "the silicon interstitial having never been identified" (Seegar et al., 1968). The reported absence of the interstitial constitutes not only a puzzling problem, but also could lead to the incorrect conclusion that interstitials do not participate in the annealing process.

An annealing of the implanted substrate is necessary to restore the dopant atoms to electrically active sites. Depending on the type of damage formed, a mild anneal of 15 min at 600°C can resotre 80% of the

dopant ions to electrically active substitutional sites. However, for certain damage conditions this figure is as low as 10 to 15%. Electron microscopic examination of the silicon after the annealing treatment reveals the presence of many small defects in high densities.

In this thesis, the type of damage is correlated with the defects formed and a study is made of how the defects affect electrical conductivity during annealing. The several previous electron microscopic studies are fraught with contradictions arising in part from the differences in interpreting complex images of the small defects and the several factors affecting their formation. This situation together with the fact that no simple model exists to explain the origin of the defects inspired this study.

1.2. Summary of Previous Investigations

1.2.1. Type of Damage Expected. Critical Dose Calculations.

The type of damage the substrate suffers depends on the dominant energy loss mechanism of the incoming ion. For small ions (e.g., boron) much of the initial loss of energy is due to electronic stopping, resulting in ionization but not gross damage. As the ion slows down, its cross section for atomic collision increases until it suffers a nuclear collision leading to massive displacement damage. This results in a damage free path followed by a zone of displaced atoms near where each ion came to rest. At the critical dose these isolated damage clusters overlap to form a buried amorphous layer. Continued irradiation then causes the buried amorphous layer to grow towards the surface (Crowder, Title 1970). For heavy ions (e.g., antimony) nuclear stopping dominates the whole range and displacements occur all along the ion path. The damage zones quickly join up to form a continuous amorphous layer extending to the surface.

The case for phosphorous is intermediate between that of boron and antimony. At 100 kV the projected range, R_p, is 1228Å with the spread, ΔR_p, equal to 350Å (Gibbons 1969). R_p is usually taken as the peak position of a Gaussian profile. The dose of P^+ ions required to drive the silicon amorphous may be estimated (assuming no vacancy diffusion) by assuming that all the target atoms are displaced. The development follows that suggested by Morehead et al. 1970. That is,

$$Do = \bar{E} n_2 \frac{dE}{dx}^{-1} \ cm^{-2}$$

where Do = dose to drive target amorphous in ions/cm^2

$\bar{E}$ = displacement energy for silicon ≃25 eV

n_2 = number of target atoms per cm^3 ≃ 15 10^{22} atoms/cm^2

$\frac{dE}{dx}$ = energy independent nuclear energy loss per unit length

$\frac{dE}{dx}$ is found by the Nielson equation

$$\frac{dE}{dx} = 7\times10^8 \times g_2 \times z_1^{2/3} \times \frac{M_1}{M_1 + M_2} \quad \text{eV/cm}$$

where z_1, z_2, M_1, M_2 are atomic numbers and masses of projectile and target (P and Si respectively). That is,

$$z_1 = 15,\ M_1 = 31 \text{ for P}$$

$$z_2 = 14,\ M_2 = 28 \text{ for Si}$$

and

g_2 is the density of silicon = 2.33 g/cm^3

giving $\frac{dE}{dx}$ = 5.1×10^9 eV/cm. Thus,

$$\text{Do} = 25 \text{ eV} \times 5\cdot10^{22} \frac{\text{atoms}}{\text{cm}^3} \times \ 5.1\times10^9 \left(\frac{\text{eV}}{\text{cm}}\right)^{-1}$$

$$= 2.4\times10^{14} \text{ ions/cm}^2$$

This estimate is in good agreement with the experimental results of Do = 1×10^{15} ions/cm^2 for 280 keV P^+ (Crowder, Tittle 1970) and 3×10^{14} ions/cm^2 for 50 keV P^+ ions (Mayer 1971). From these estimates it is reasonable to conclude that for the foils used in this study, which were 100 keV P^+ ions implanted in the 10^{14} range, a continuous damaged layer was not formed. A high density (>5×10^{11} per cm^2) of almost overlapping damage clusters about 70Å in diameter (Mazey, Nelson, Barnes 1968) are expected.

The structure of the damage cluster itself is unclear. Parsons (1965) and Mazey et al. (1968) using electron microscopic studies show that these clusters consisted of a central disordered core surrounded by a sheath of crystalline material containing a large number of defects. Infrared absorption and EPR studies (Stein 1969, Daley 1969) show the presence of about five divacancies per implanted ion. The rest, over 95%, not detectable by their method, they concluded were incorporated in the damage core. A volume expansion of 2% accompanies the crystalline to amorphous transition (Tu et al., 1972). An expanded amorphous region is then under hydrostatic compression from the surrounding perfect crystal. The stress using Hooks law is expected to be $\sim 10^9$ dynes/cm^2. Comparable values (2×10^9 dynes/cm^2) have been reported by Ernisse (1971).

The number of atoms displaced per phosphorous ion is about 1000 (Gibbons 1972). Thus 10^{22} atoms are expected to have been displaced per cubic centimeter. A large number of the resulting Frenkel pairs probably annihilated. Assuming that 90% of the pairs annihilate, 10^{21} defects per cubic centimeter are expected.

1.2.2. The Annealing of Damage

Upon heating, the remaining damage repairs and the implanted phosphorous atoms come to occupy substitutional sites. This process, occurring in the 200-600°C temperature range, is accompanied by the disappearance of the divanancy and vacancy-group V complexes (Mayer 1971). Thus the recovery of electrical activity has been associated with the annealing of vacancies (Mayer 1968). It is tempting to conclude from this that the divancancies collapse to give the defects observed after the annealing treatment. However, vacancy type defects are not observed after the annealing treatment (Jenkins et al. 1973, Seshan et al. 1974).

The percentage of the implanted ions that are electrically active after a certain given anneal depends critically on the damage. For phosphorous ion implantations, when a continuous amorphous layer is formed, a mild anneal for 15 min at 600-700°C restores almost 100% activity. When a continuous layer is not formed (dose $>10^{13}$, $<10^{15}$ ions/cm^2) the same annealing treatment results in less than 15% activity. A much higher annealing temperature of 900°C is required to recover full electrical activity (Crowder 1960, Gibson et al. 1968).

1.2.3. Electron Microscopy Studies

Several electron microscopic studies of the defects formed upon annealing of ion implanted silicon in the 500-700°C range exist. They are, however, incomplete and advance contradictory descriptions of the defects and suggest no model for the defect formation. The defects in boron implanted silicon were first reported as vacancy type (Chadderton, Eisen 1971) assuming that they are formed from the collapse of divacancies. Another study (Bicknell, Allen 1970) reported that the defects were interstitial type.

One study of defects in phosphorous implanted silicon first reported that they were perfect loops lying in the foil plane and were interstitial type (Davidson, Booker 1970). Others also reported the loops as perfect but the habit planes were not determined (Tamura et al. 1971, Wu et al. 1973). Recently all these loops have been reported as imperfect loops (i.e., Frank loops) lying on the four {111} planes (Jenkins et al. 1973, Madden 1973). There has also been considerable variation in descriptions of loops morphology between workers. Linear defects were first reported as absent in phosphorous implants (Bicknell, Allen 1970) while others

have reported their presece (Seshan et al. 1972, Madden 1973).
Tamura et al. (1971) found linear defects in hot substrate phosphorous implants only.

It was evident from this situation that a more systematic study of the nature of the defects was warrented.

1.3. Discussion. Topics Investigated

From the brief review presented, it is obvious that several factors affect the annealing process; how these affect the recovery of electrical properties and influence the kind of defects produced is not completely understood. The situation in silicon is further complicated not only by the dopants in the foil prior to implantation but also by impurities like oxygen and carbon (present in concentrations about $10^{15}/cm^3$) whose role is entirely unknown.

This electron microscopic study was undertaken in order to clarify the specific problems listed below. Phosphorous and silicon ions were chosen for the bombarding species as boron implantations have been more thoroughly investigated.

Firstly, in the light of conflicting reports about the nature of the defects, a further study of defect type, habit plane and morphology was thought necessary. In order to do this the behavior of the images of these small defects were first studied and the conditions under which the best images were obtained were determined using the low as well as the high voltage electron microscopes.

Secondly, the poor electrical activity of phosphorous implantations up to a dose where a continuous amorphous layer is formed (Crowder et al., 1969) does not have a satisfactory explanation. Precipitation near the loops has been suggested but no mechanism has been proposed (Davidson and Booker, 1970). Attraction of the dopant to the dislocation core is a possibility (Gibbons, 1970). However, this interaction, varying as the square of the difference between the volumes of the host and impurity, is expected to be small for phosphorous in silicon.

Lastly, there is no simple model for the annealing process. It is suggested on the basis of observations that the annealing occurs via the motion of vacancies and divacancies (Cheng et al., 1966). How this results in the formation of high densities (10^{13} per cm^3) of small interstitial type dislocation loops has no simple explanation. A model to explain this result has been developed.

CHAPTER II.
SPECIMEN PREPARATION

2.1. Implantation Procedure 15

2.2. Heat Treatment 18

2.3. Thin Foil Preparation 19

"Unhurt amidst of war of elements, the wrecks of matter and the crash of worlds."
Addison

2.1. Implantation Procedure

A schematic of the ion implantation procedure is shown in Fig. 2.1. The implantation was carried out at the Fairchild Research and Development division. The foils were tilted 8° away from the exact 111 orientation in order to minimize channeling. Ions of P^+ and Si^+, accelerated to 100 keV were implanted into the following chips.

1. ⟨111⟩ p-type (boron doped) silicon. Resistivity 0.2-8 Ωcm
2. ⟨111⟩ n-type (phosphorous doped) silicon. Resistivity ~1 Ωcm
3. ⟨111⟩ n-type (antimony doped) silicon. Resistivity ~1 Ωcm
4. ⟨111⟩ n-type (phosphorous doped) Lopex or low oxygen silicon. Resistivity ~1 Ωcm.
5. ⟨100⟩ p-type (boron doped) silicon. Resistivity ~1 Ωcm.

Doses of $2\text{-}3\times10^{14}$ ions/cm^2 using beam currents of 1μ amp/cm^2 were used. A calculation shows that the implantation takes about half a minute:

$$\text{dose} = 2\times10^{14}\ \text{ions/cm}^2 = 3.2\times10^{-5}\ \text{coul/cm}^2$$
$$\text{current} = 1\times10^{-6}\ \text{coul/sec cm}^2$$
$$\text{implant time} = \text{dose/current} = 3.2\times10^{-5}/10^{-6} = 32\ \text{sec}$$

Estimates of the temperature rise due to beam heating depend critically on the volume assumed affected by the energy of the beam. If E is the energy deposited by the beam in 32 sec

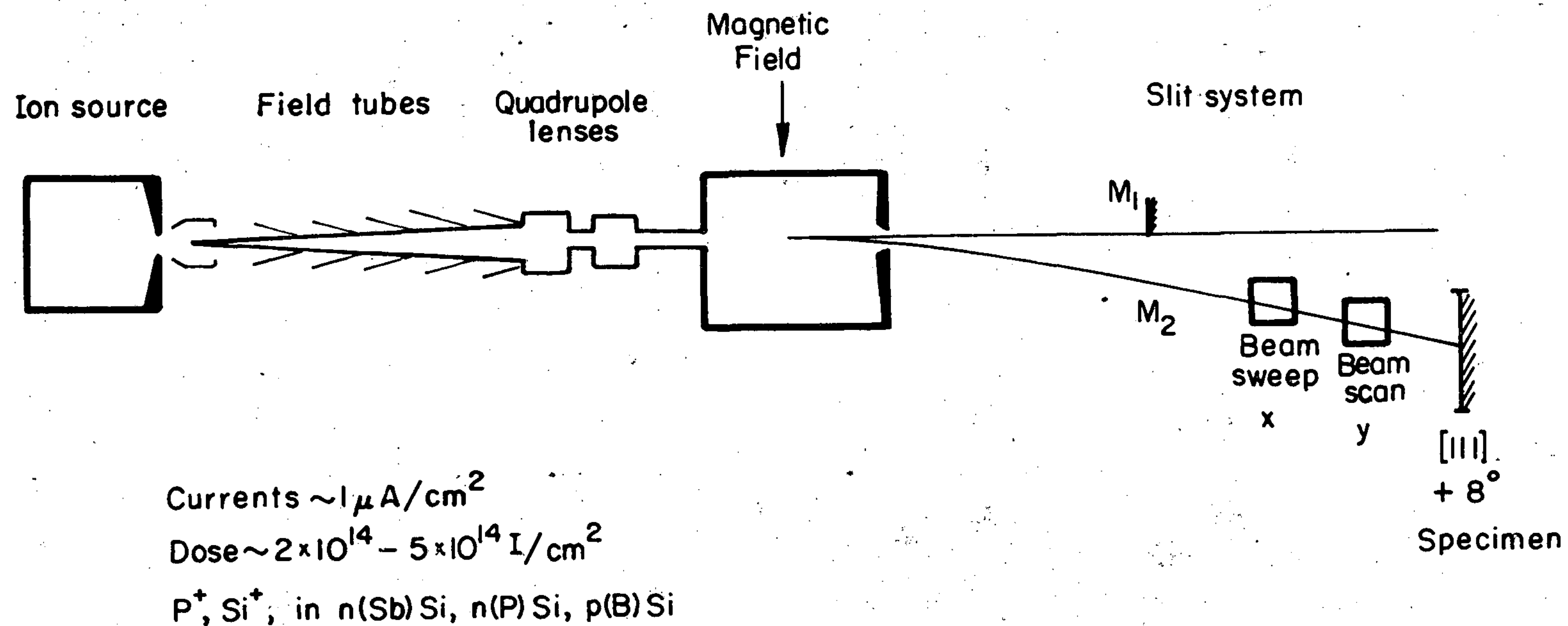

XBL744-6106

Fig. 2.1. The ion-implantation equipment showing the ion source and the accelerating tubes. The mass analyzing magnet separates ions of one mass e.g., P^{+}_{31}. The x,y beam sweeps scan the ion beam across the specimen. Polished wafers of ⟨111⟩ silicon, tilted 8° away from the exact ⟨111⟩ direction in order to minimize channelling, were used.

$$E = tVI = (32 \text{ secs})(10^5 \text{ volts})(10^{-6} \text{ amps/cm}^2)$$
$$= 3.2 \text{ watts sec/cm}^2$$
$$= 0.768 \text{ cal/cm}^2$$

Assuming that all this heat is retained in a volume of one square centimeter by 2000Å (range of the ion) the temperature rise ΔT is related to E by

$$E = m \cdot C_p \cdot \Delta T$$

where m is the mass = 2.10^{-5} $cm^3 \times 2.3$ g/cc = 4.66×10^{-5} gm

C_p is the specific heat = 0.162 cal/g°C for silicon

giving

$$\Delta T = \frac{0.768}{0.755 \times 10^{-5}} \simeq 10^{+5} {}^\circ C \quad .$$

Allowing for an increase in volume affected by over two orders of magnitude a temperature rise of about 500°C is still expected.

The importance of effective cooling during implantation is obvious from this calculation. The chips used in this study were clipped on to an aluminum block during implantation and a temperature rise of over 50°C was not noticed (Reddi, 1974). Other procedures are possible, such as making an indium base contact to provide good heat conduction (Crowder, 1974). That sample heating is one of the factors which affect whether or not linear defects form is a result of this study (see Chapter V).

2.2. Heat Treatment

Prior to heat treating the foils they were glued down on a glass slide, implanted side down, with heated wax and discs 2.3 mm in diameter were cut and dished in the middle using a ultrasonic cutter. The discs were removed after cutting and dishing by remelting the wax, and cleaned by soaking in 111 trichlorocthylene which dissolves the wax. The discs were then heated in a fore-flushed ABAR induction furnace in a static atmosphere of extra pure helium. In order to check that no impurities were diffusing into the samples another batch was encapsulated in pyrex tubing in a 96% He 4% H_2 atmosphere. These capsules were heated in a tube furnace. One batch was fast cooled by plunging the capsule in cold water. Subsequent microscopic analysis failed to reveal any significant difference in defect morphology between these three different batches.

2.3. Thin Foil Preparation

After the discs were heat treated they were chemically thinned in a 3:1 mixture of two solutions A and B; A was a mixture of 3:1 hydrochloric acid and nitric acid and B was a solution of 2.5 g iodine in 1000 ml of acetic acid. The implanted surface was protected from the solution by sticking the discs, implanted surface down, on the sheets of PTFE. Hot wax was used to stick the specimens. The temperature of melting of the hot wax was ~65°C. Some annealing is expected to occur at this stage. Thin foils, in the 4500Å thickness range, were produced by stopping chemical polishing when a perforation was first seen. A light source was used to aid early detection. The samples were removed using 111-trichloroethylene and washed in acetone and alcohol before examination.

CHAPTER III.
OPTIMUM IMAGING CONDITIONS AND IMAGE COMPLEXITIES

3.1. Introduction 21

3.2. Experimental Results 23

3.2.1. 650 kV Optimum Conditions and Complexities 23

3.2.2. 100 kV Optimum Conditions and Complexities 27

3.3. Discussion and Conclusions 36

"Nature is often hidden, sometimes overcome, seldom extinguished." Bacon

3.1. Introduction

Defects produced after the annealing of ion bombardment damage are small (in the 200-500Å range) and present in high concentrations (over 10^{15} defects/cm^3). Conventional bright and dark-field images (Fig. 3.1a,b) are wide (about 200Å), dominated by strain field effects, and bear no relation to the true shape and size of the defects. Consequently, conventional imaging techniques were of little value in characterizing these defects.

Several nonconventional electron microscopic methods aimed at reducing image width have been announced in the recent years: the weak-beam method (Cockayne et al., 1969), the bright field systematic method (Osieski et al., 1971) and the symmetric weak-beam bright field method (Kelly et al., 1973). It was obvious that such methods could be used to advantage in characterizing the defects in ion implanted silicon.

Since no systematic study exists, it was deemed necessary to determine the best imaging conditions for these defects at 650 kV and at 100 kV. An experimental method was used. Thin foils were gradually tilted in the electron microscope from the (0,g) to the (0,4g)* diffracting condition and the bright field and weak-beam (±g,ng) images were recorded.

*The notation used for denoting a certain diffraction condition is as that used by Humphreys et al., 1973: (g,ng) denotes an image using g with the Ewald sphere passing through ng. (0,ng) is the bright-field image, (-g,ng) is the weak-beam image etc.

Several interesting trends and complications in image behavior were observed.

In order to simulate the observed behavior of the images, computations of image profiles of closely spaced dipoles under systematic conditions have been performed (Chen, 1974). A majority of the trends have been explained (Chen et al., 1974) with the notable exception of the anamolous disappearance of some images in bright field.

3.2. Experimental Results

3.2.1. 650 kV Optimum Conditions and Complexities

The images in Fig. 3.2.1 and the traces across the defects show the reduction of image width that exciting combinding good defect visibility with a reasonably narrow image occurs for the (0,2gs+) bright field condition, Fig. 3.1.1b and the g,2gs+ weak beam condition for g = 220 as in Fig. 3.1.2b. Although exciting higher orders of reflection decreases image width, contrast above background drops over 60% (Fig. 3.1.1d) so that the defects can hardly be seen. The bright field systematic images require shorter exposures than the weak beam images; the latter yield three times more contrast for the same imaging condition.

Experiments showing that the optimum imaging condition for g = 111 is the (0,3gs+) bright field and the (g,3gs+) dark field is shown in Fig. 3.3e and f respectively. These images also show the great sensitivity of the images of small defects to the diffracting condition when several beams are excited. The circled loop is seen, in bright and dark fields, at the exact Bragg conditions (0,3g) and (g,3g) only: Fig. 3.2c and d. Because of this anamalous disappearance effect caution is necessary before concluding that a certain defect is absent when several beams are excited. Another complicating feature in high voltage images may be seen in Fig. 3.2.1c where the line of no contrast of some loops are seen to rotate as G is changed slightly: for instance at loops as well as that adjacent to the rod R. Such rotations could lead to incorrect assignments of the Burgers vector specially if specific two-beam models e.g., Bell and Thomas (1965), are used.

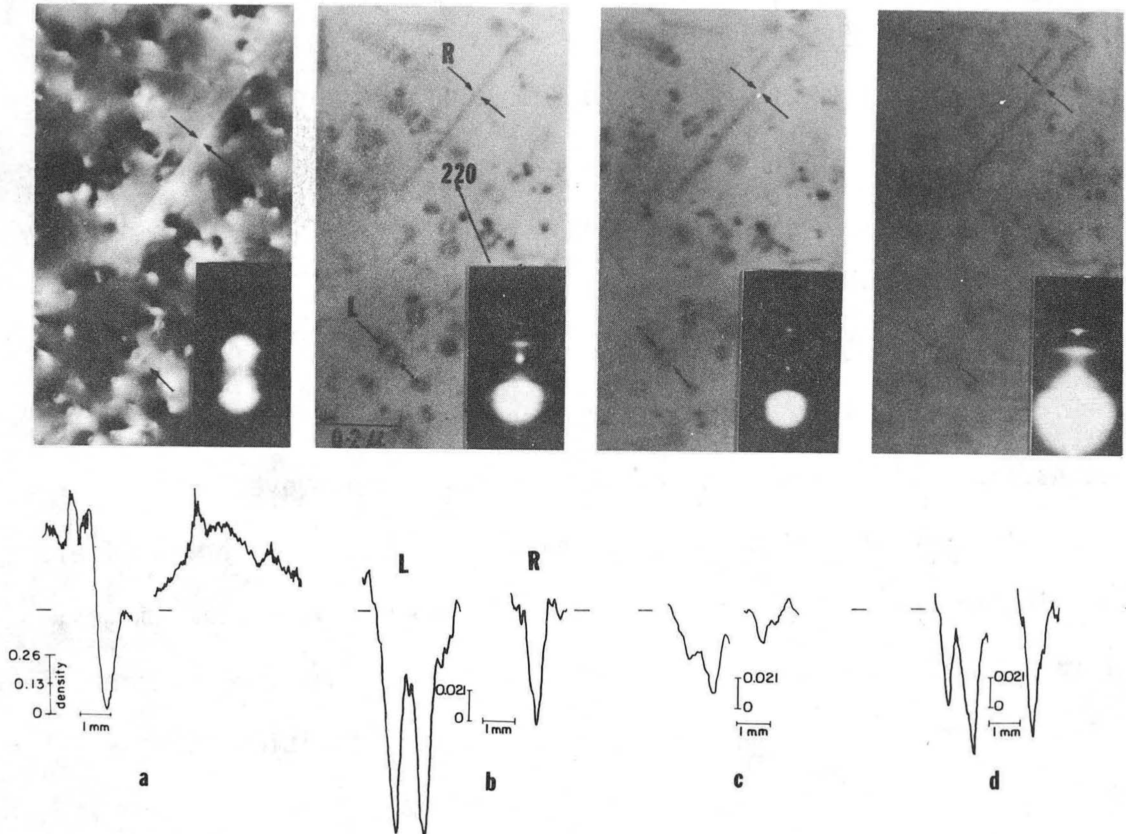

XBB 7210-5179

Fig. 3.1.1. Images in bright-field with g = 220 at 650 kV for the following conditions: a. (0,g), b. 0,gs+), c. (0,2g), d. (0,2gs+). Shown below are densitometer traces across the loop L and the "rod-like" defect R. The best visibility condition with narrow images was at d: (0,2gs+). Further tilting resulted in a great loss of visibility.

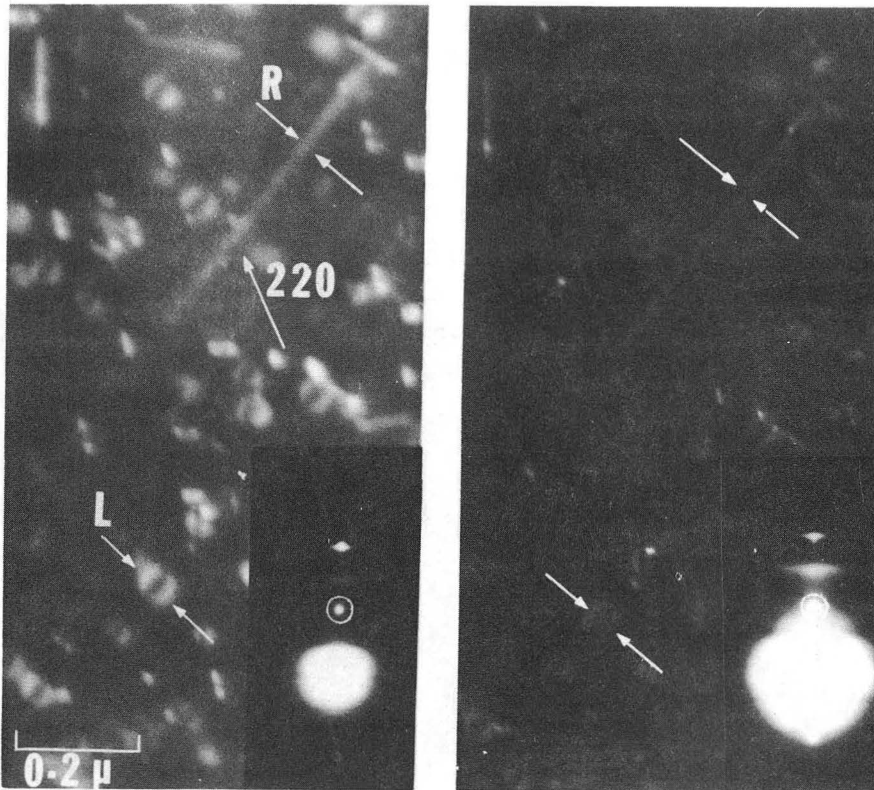

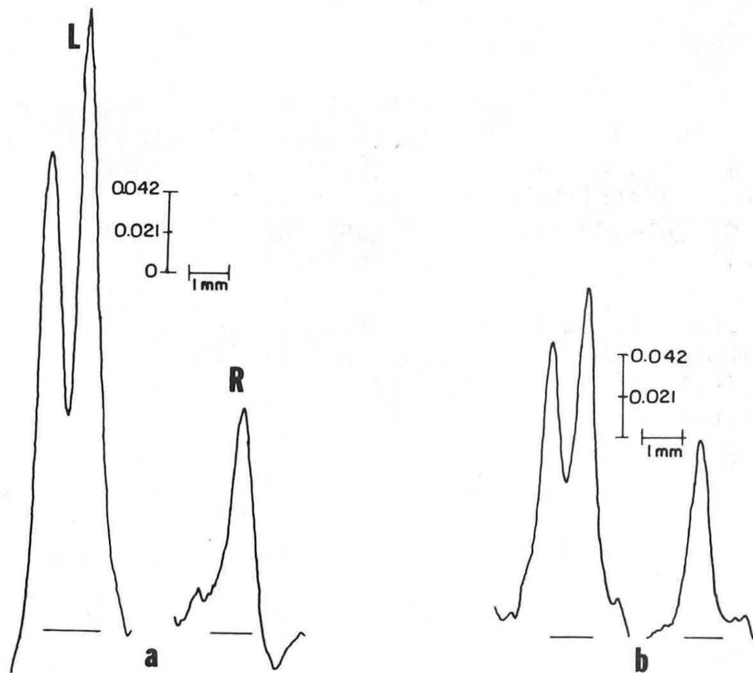

XBB 7210-5178

Fig. 3.1.2. The same area as in Fig. 3.1.1 in dark field under the following conditions: a. (g,2g), b. (g,2gs+), and the traces across L and R. This figure illustrates the increase in visibility of dark-field images over bright field images under the same diffracting conditions (c.f. 3.1.1d). These images, however, require much longer exposure (~16 sec).

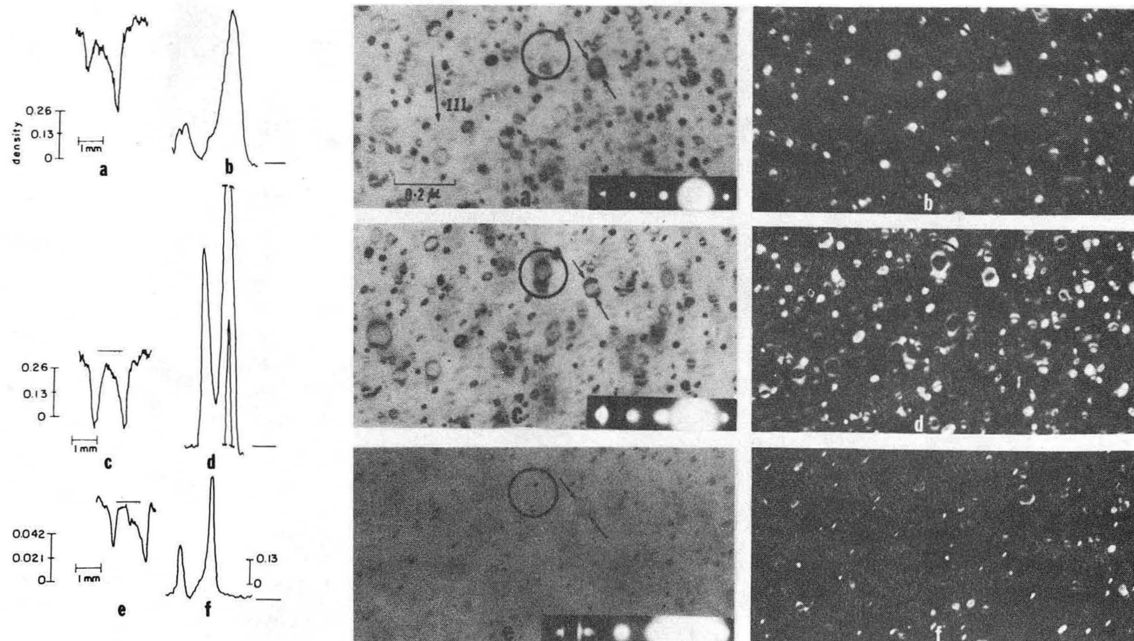

Fig. 3.2. Images in bright- and dark-field with g = 111 at 650 kV for the following conditions: a. (0,2gs+), b. (g,2gs+), c. (0,3g), d. (g,3g), e. (0,3gs+), f. (g, 3gs+). This figure illustrates that the visibility of the defects in bright and dark field can change dramatically for small changes in diffracting condition (c.f., a,c or b,d). The circled loop "anomalously" disappears except at the extract Bragg condition (c and d). Computer calculation (Chen et al., 1975) shows that visibility can also be affected by effective foil thickness and defect size.

3.2.2. 100 kV Optimum Conditions and Complexities

Experiments to determine the optimum conditions at 100 kV are shown in Fig. 3.3. The images and the microdensitimeter traces show that the edges of the loop are best resolved for the (0,1gs+) g = 220 diffracting condition (Fig. 3.3c). For g = 111 the (0,2gs+) condition was found optimal.

The great enhancement of image detail, the reduction of image width and the increase of accurate information about loop size, shape and habit planes available in weak-beam images is seen in Fig. 3.4. The reason for this is explained in excellent reviews by Cockayne (1973) and is briefly given below. Image widths are to a good approximation of the order of $\xi_g^s/3$, where ξ_g^s is the effective extinction distance, and

$$\xi_g^s = \xi_g^o / \sqrt{1 + \omega^2}$$

where ξ_g^o is the extinction distance for a certain g and ω = dimentionless deviation. If two beams (0,g) are excited and the -g beam is imaged, ω of this beam is large as it lies outside the Ewald sphere. This makes ξ_g^s small (~60Å) and image widths of ~20Å are routinely obtained by this method. That the habit plane of the loops is {111}, that the loops are imperfect (Frank) loops, that they are hexagonal and in the 200Å size range can be deduced from this one image. Such images were used for the most part for the characterization of these defects.

A comparison of the accuracy with which the size of a defect amy be estimated by the bright field, symmetric weak-beam bright field (Fig. 3.5b) and weak-beam images (Fig. 3.5c,d) is shown in Table 3.1. Table 3.1 shows the advantages of the reduction of image width obtained

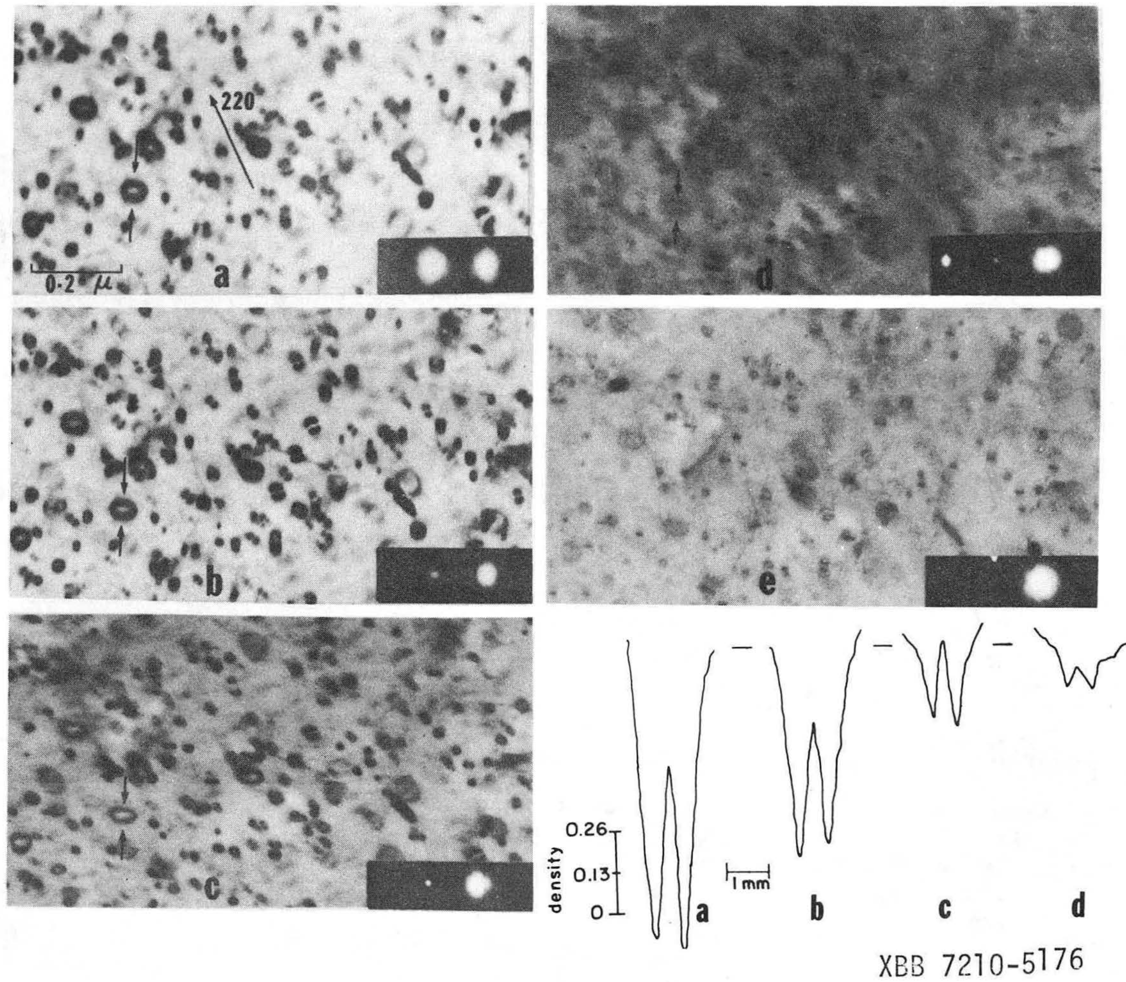

XBB 7210-5176

Fig. 3.3. Images in bright field with g = 220 at 100 kV for the following conditions: a. (0,g), b. (0,gs+), c. (0,gs++), d. (0,2g), e. (0,2gs+). Also shown are microdensitometer traces across a loop. The best visibility and narrowest images were obtained for the (0,1gs++) condition (c).

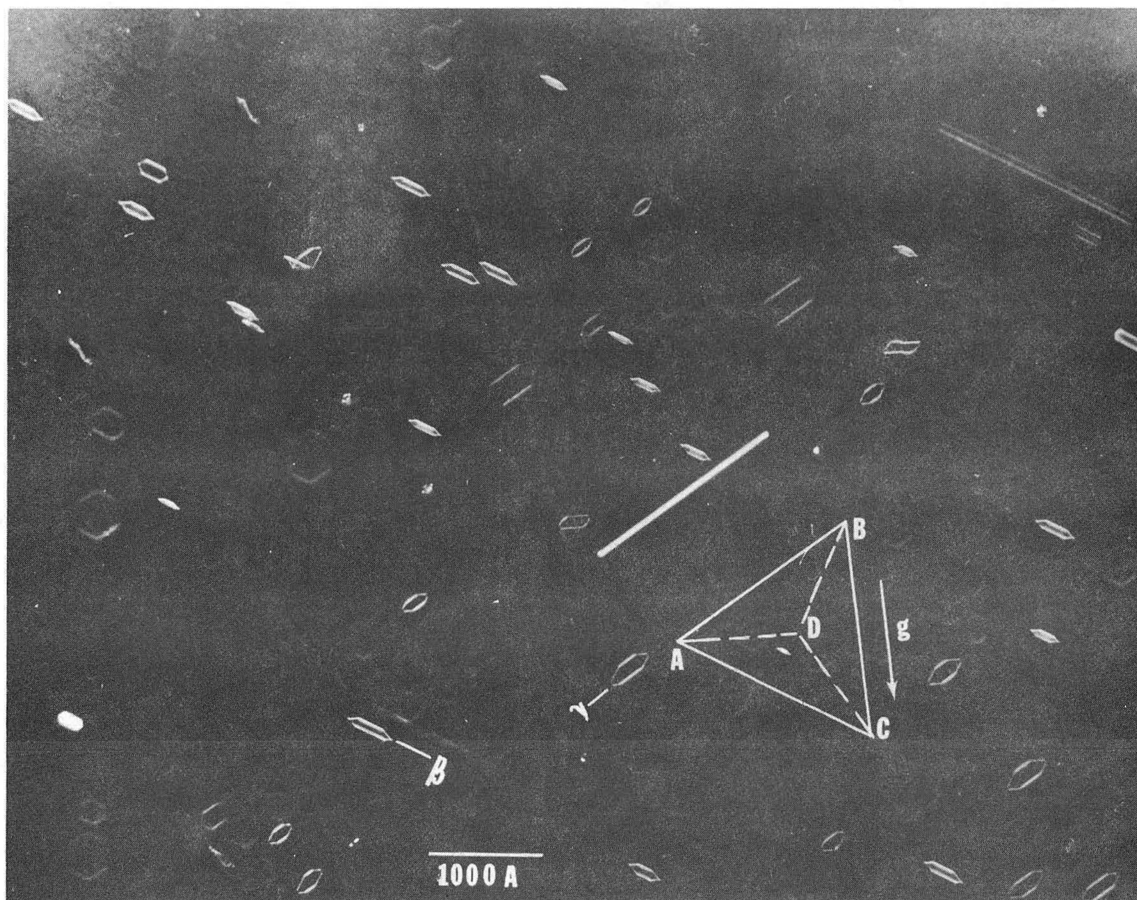

XBB 747-4427A

Fig. 3.4. A weak-beam image (-g,3gs+) at 100 kV. This figure illustrates the great enhancement of image detail the weak-beam technique affords. This one image with the Thomson tetrahedron shown can be used to conclude that the habit planes of the loops are {111} as marked, that the loops are imperfect (Frank) loops and that they are hexagonal in the 200-300Å size range.

Fig. 3.5. A comparison between images in bright field (a), in the symmetric-weak-beam-bright-field (b) and in weak beam (g,3g) c, and (g,4g) d. The SWBBF image requires shorter exposure than the WB images, and produces double images (c) if the loop is faulted or single images if it is perfect (B). The weak-beam images require longer exposures and give reliable dimensions of defects within ±5Å.

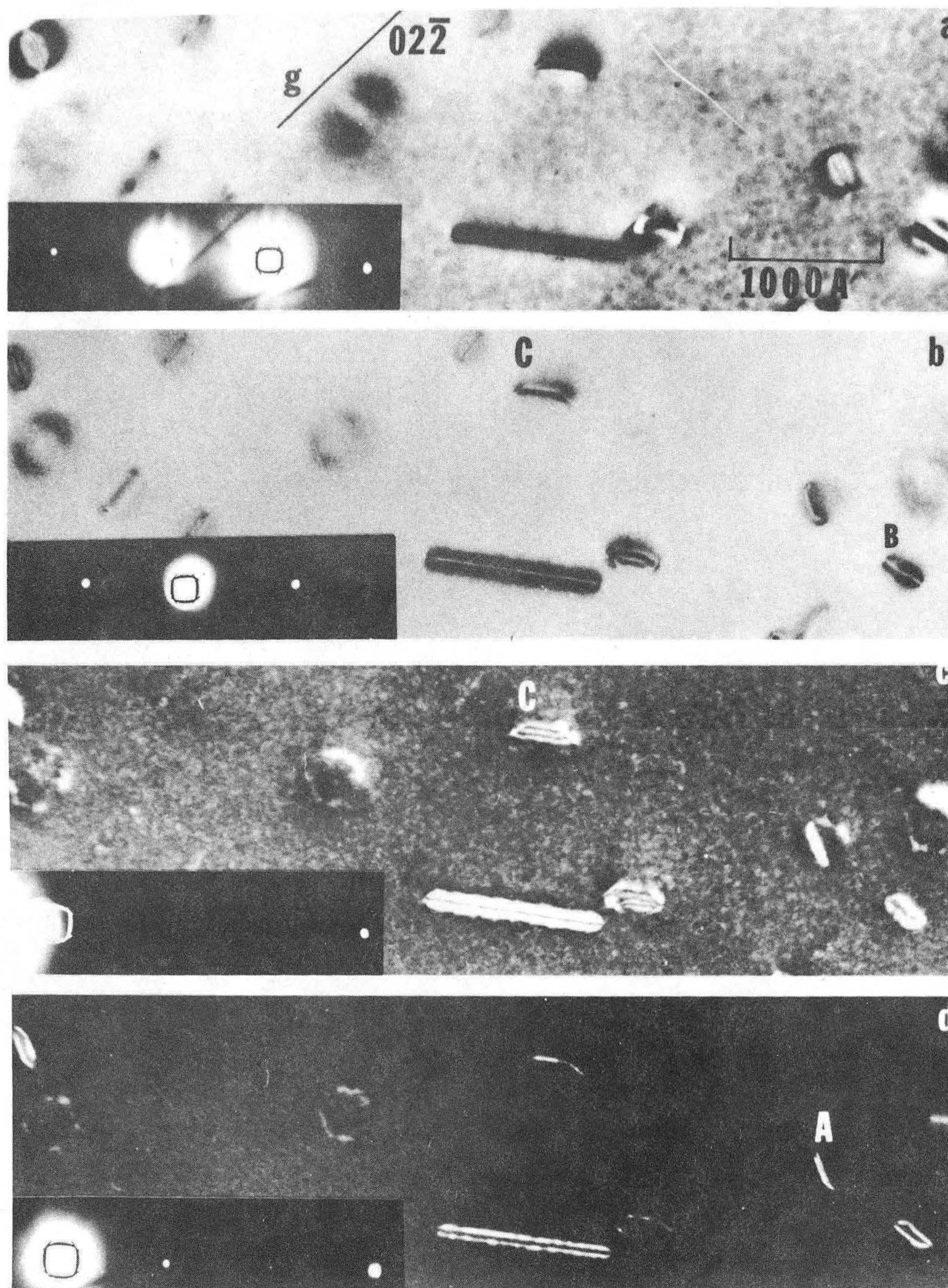

XBB 742-1267

Fig. 3.5

Table 3.1. Image width and estimated width of defect B.

Fig. 3.6	a	b	c	d
Image Width Å	600	60	55	28
Estimated Width of Loop B Å	undefined	98	110	60

by the symmetric-weak beam method (Fig. 3.5b) and weak-beam methods (Fig. 3.5c and d) over the conventional bright field image (Fig. 3.5a). In this case this has been used to determine the width of the loop B (Seshan, 1974).

The symmetric weak-beam bright field method requires shorter exposure times (~15 secs) than the weak-beam method (~60 secs). It has also proved useful in quickly determining the ratio of faulted to perfect loops (see Chapter IV, p. 63).

Nonconventional images at 100 kV were also found to suffer from image complications arising from the interaction of several beams. This may be seen in Fig. 3.6a,b. Figure 3.6a shows a bright field and Fig. 3.7a,b (+g/-g) weak-beam of the same area. In the weak-beam image (Fig. 3.7b) just below the hexagonal loop marked g the faint image of a linear defect may be seen; this lies along a [110] direction $\overline{AC}$ according to the Thomson tetrahedson in Fig. 3.7a.

The image of this defect is not seen in the bright field image (Fig. 3.7a). The absence of the rod in the bright-field image, Fig. 3.7a, and its presence in the weak-beam image (Fig. 3.7b) confirms that 100 kV bright field images are liable to the anamalous disappearance effect. The computer simulations (Chen et al., 1974) show this could arise from defect position in the foil defect width, foil thickness and diffraction conditions.

Fig. 3.6. Shows a bright-field and weak-beam image of the same area. The figure shows that the visibility of the defects, even in bright field, is very sensitive to the diffracting condition. For example, the linear defect at M, visible in the W-B image has "anomalously" disappeared in the B-F image. The figure also shows the four sets of Frank loops marked with respect to the Thomson tetrahedron.

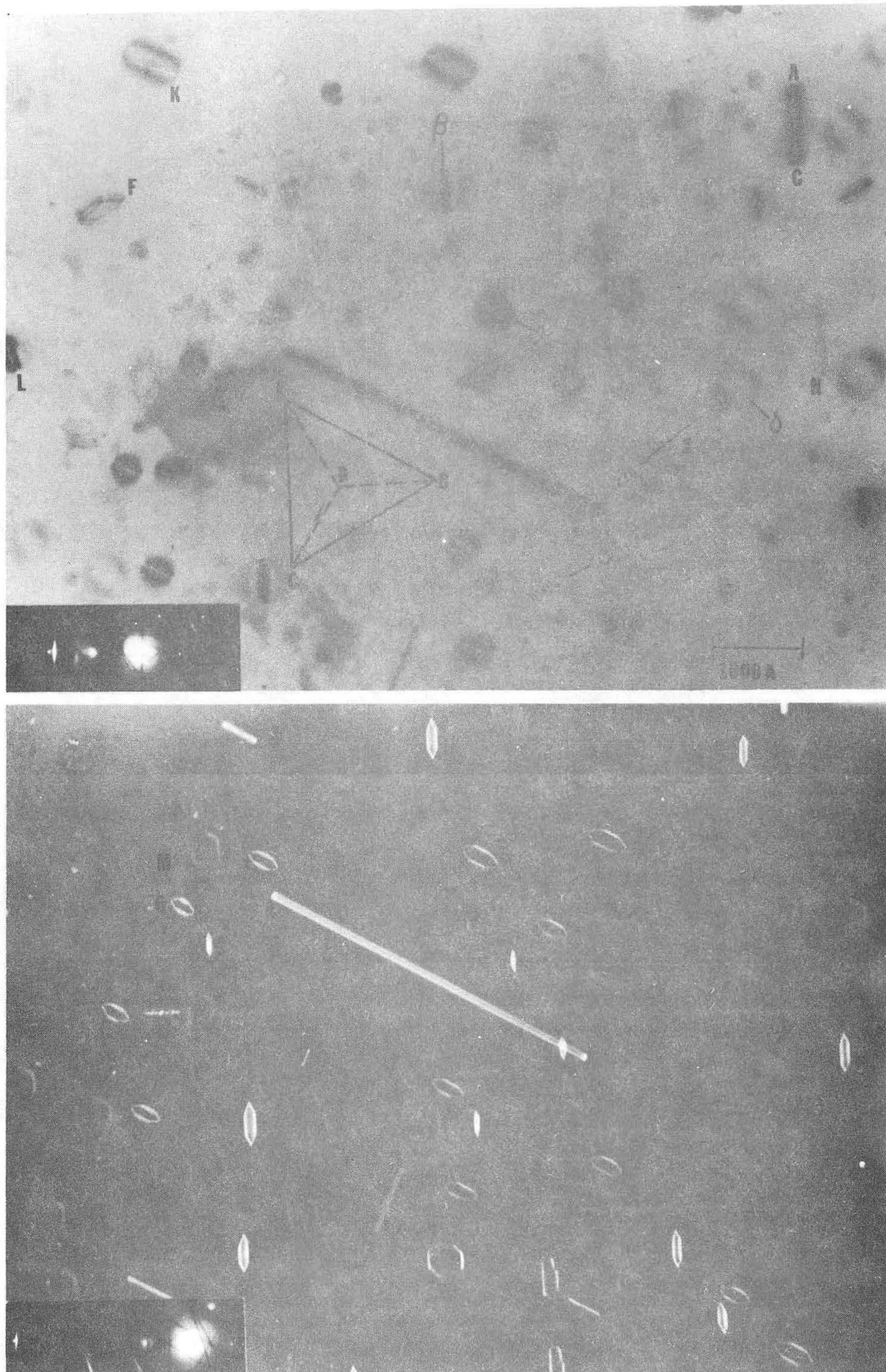

XBB 747-4425

Fig. 3.6

3.3. Discussion and Conclusions

One common feature observed in the 100 kV and 650 kV bright and dark field images is the anamalous disappearance effects for small changes in the diffracting conditions. Further, a definite trend in the optimum conditions for resolution of the images were seen as shown in Table 3.2.

In order to explain these trends the images of closely spaced dipoles (60-500Å) in silicon for the systematic cases with up to seven beams excited using the Howie-Basnski (Howie and Basinski, 1968) were computed. From these profiles the visibility defined as:

$$\text{visibility} = (I_{max} - I_{min}/I_{max} + I_{min}) \quad ,$$

was determined (Chen, Seshan and Thomas, 1974). This quantity was found to drop from 0.8 to 0.1 for changes in sg the deviation parameter of 2%. Such a variation exactly duplicates the behavior of images such as that in Fig. 3.3 and 3.7.

The visibility was also found to vary with size and depth of the defect in the foil and quite markedly with foil thickness. Stereo-microscopic data show that the rods seen in Fig. 3.8 are distributed over a depth range of 2000Å. It is, therefore, quite likely that the disappearance effect is related to the defect size and depth in the foil. It is known that weak beam images are sensitive to the depth of the defect in the foil (Perrin and Eyre, 1973). This study shows that bright field images of small defects in silicon suffer the same effect at 100 and 650 kV.

Optimum imaging conditions--experimental and theoretical.

kV	g	BFS Optimum Condition	Condition of Maximum Transmission Humphreys et al., 1971 at 1 MeV
100	220	(0, 1g s+)	(0, 1g s+) 100 keV, most metals
	111	(0, 2g s+)	(0, 2g s+)
650	220	(0, 2g s±)	(0, 2g s±) 1 MeV, light elements
	111	(0, 3g s±)	(0, 3g s±) 1 MeV, light elements

As may be seen in Table 3.2, there seems to be a relation between experimentally determined optimum conditions and the conditions for good transmission as determined by Humphreys, Thomas, Lally and Fisher, 1971. For instance, they determine from Bloch wave intensity calculations that the conditions for best transmission for light elements in bright field with g = 220 is just positive or negative of the second order Bragg position; this is also the best imaging condition in Fig. They find that conditions of good transmission at 100 kV are poor transmission conditions at 1 MeV; in the study of images it is seen that the (0, 1gs+) condition which is the optimum condition at 100 keV, Fig. 3.4c, is a poor imaging condition at 650 kV, Fig. 3.2.1b. Although these studies suggest a connection between electron penetration and image contrast, the detailed mechanism has not been worked out.

Non conventional images at 100 keV were found to have the required resolution to characterize these defects and were used for the most part. The only limitation was that thin areas of the foil (2-3000Å) had to be used. This may yield misleading information about defect depth distributions as the defects are expected at depths up to 4000Å in the foil. Therefore, for stereo macroscopic work relating to the depth distribution of the defects high voltage images, where thicker foil sections (8000-10,000Å) could be imaged, were used.

CHAPTER IV.
CHARACTERIZATION OF THE DEFECTS

4.1. Introduction 40

4.2. Characterization 42

4.2.1. Determination of Habit Planes 42

4.2.2. Determination of Defect Type 49

4.2.3. Depth Distribution and Contrast Effects 57

4.3. Defect Morphology-Silicon Prehistory 62

4.4. On the Presence of Linear Defects 44

4.5. Discussion and Conclusions 72

"He's got 'em on the list, he's got them on the list
And they'll none of them be missed, none of them be missed." Mikado

4.1. Introduction

An unambiguous characterization of the defects formed upon annealing ion-damaged silicon is necessary before a model for their formation is proposed. Contradictory descriptions of their nature have been advanced owing probably to their small size, high densities and complex image behavior (Chapter II). The loops formed upon annealing were first described as perfect with burgers vectors of the type a/2[110]; their habit planes were, however, not exactly determined (Davidson and Booker, 1970; Bicknell and Allen, 1970; Tamura et al., 1972; Wu et al., 1974). Most of these investigators reported interstitial loops except Chadderton and Eisen (1970) and Bicknell (1973) who reported vacancy loops. More recently, using weak beam techniques a majority of the loops have been reported as interstitial and imperfect i.e., interstitial Frank loops with a/3[111] displacement (Jenkins et al., 1973).

The occurrence of linear defects in P^+ implants constitutes another perplexing problem. Such defects are observed in great abundance in B^+ implants into n-silicon. However, in P^+ implants into p-silicon they were first reported to be absent (Bicknell and Allen, 1970). They associated with this the absence of negative annealing in P^+ implants. Linear defects were present in the room temperature P^+ and Si^+ implants used in this study (Seshan and Washburn, 1972), and were also reported in high temperature implants by Tamura et al. (1972). More recently shorter linear defects than those found in B^+ implants have been reported by Madden (1973) in P^+ implanted p-silicon.

In this study, 2 10^{14} 100 keV ions per cm^2 were implanted as below:

a. P^+ ions in p (boron doped) 111, 100 silicon 0.25-8 Ωcm

b. P^+ ions in n (phosphorous doped) 111 silicon 1 Ωcm

c. P^+ ions in n (phosphorous doped) "lopex" silicon 1 Ωcm

d. P^+ ions in n (antimony doped) 111 silicon; 1 Ωcm

e. Si^+ ions in p (boron doped) 111 silicon; 1 Ωm

It is shown in Chapter I, part 1.2.1, that the dose used was below that required for the onset of a completely amorphous layer and that a high density of isolated amorphous or disordered zones are expected.

In this chapter the determination of the habit planes of the defects are described by large angle tilting and by the calculation and comparison of some inclination dependent contrast features in Section 4.2.1. Whether the defects on the inclined planes and those in the foil plane are interstitial or vacancy is determined in Section 4.2.2. In Section 4.2.3 the depth distribution of the defects found by stereomicroscopy is described. Some unusual contrast features exhibited by the loops are also discussed. In Section 4.3 the effect of silicon prehistory on defect morphology is described. In Section 4.4 some experimental observations on the linear defects are presented.

4.2. Characterization

4.2.1. Determination of Defect Habit Planes

The habit planes of large loops an simply be determined by tilting the foil to orientations where the defects appear edge on. The images of small defects, however, are so dominated by their strain fields that images under conventional contrast conditions are insensitive to changes in orientation; see Fig. 4.4 for example.

In weak-beam images changes of loop orientation are more readily visible (Fig. 4.1). A special wedge was constructed in order to effect this tilt in the Philips EM 301 high resolution instrument. In Fig. 4.1(a) a 111 foil is tilted to the 112 pole where one of the loop variants, β, appears edge on. In Fig. 4.1(b) a similar foil is tilted to the [233] pole. Consistent with the view that the defects lie on {111} planes, the varient appears flatter. In Fig. 4.1 the tetrahedron of {111} planes is shown with the Thomson notation.

If the displacement vector of the defects is a lattice vector their images should show displacement fringe contrast as seen in Fig. 4.2. This together with their symmetrical hexagonal shape is positive evidence that the loops are Frank loops, and inclose a stacking fault. Their hexagonal shape is indicative of the fact that they are in growth stages where jog nucleation is the critical step (Friedel, 1969) and that the Frank dislocation inclosing the stacking fault is split into a stair rod and a Shockley partial dislocation (Hirth and Lothe, 1973).

The fringe spacing p is related to the effective extinction distance ξ_w^g and the inclination θ of the defect to the foil surface by

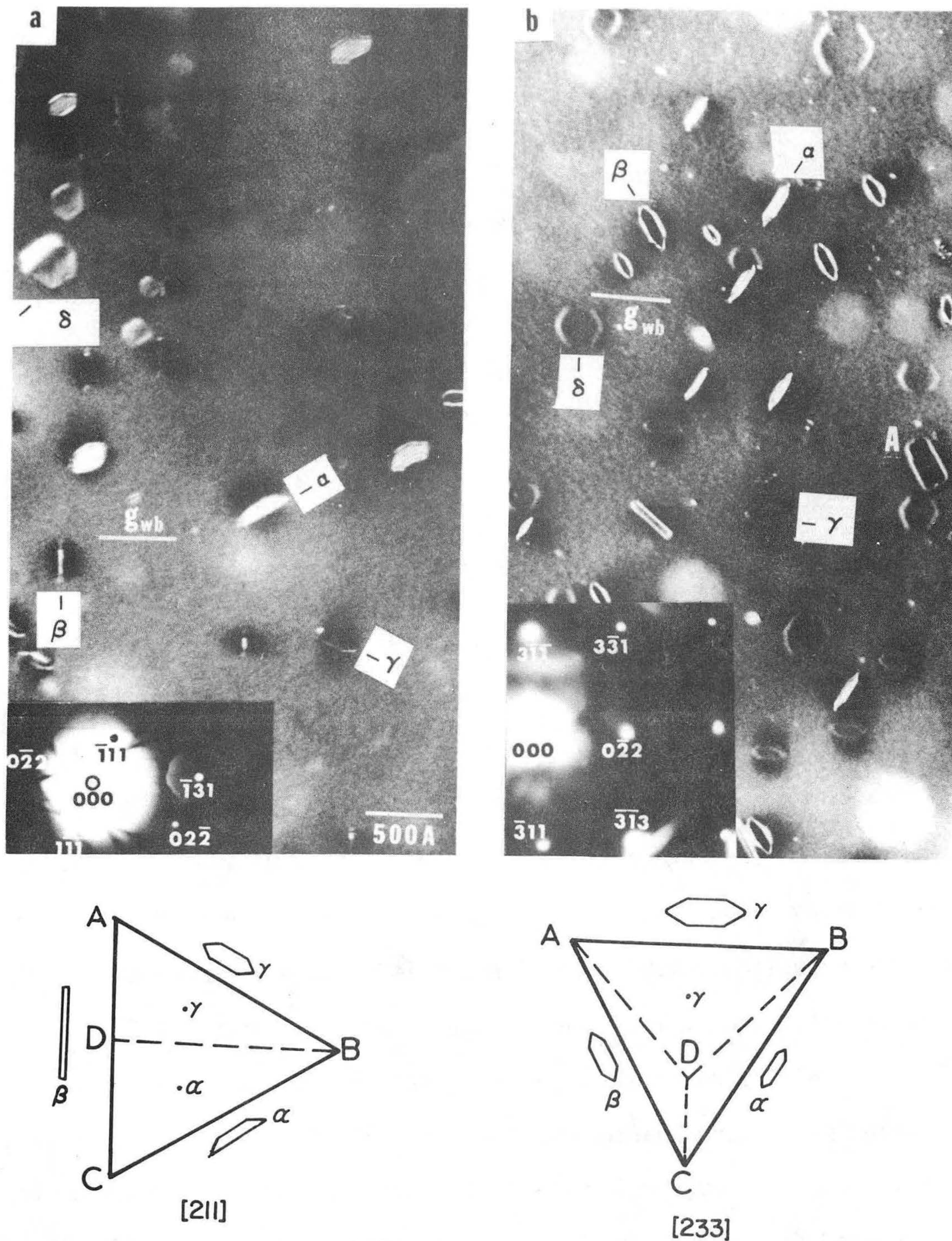

XBB 745-3335

Fig. 4.1. (a) Weak-beam image of 211 and (b) at 233. The Thompson tetrahedron corresponding to these poles is shown. At the 211 pole the β varient of the Frank loop should appear edge-on as is the case (a). At the 233 pole the γ varient should appear slightly larger in projection than α and B as is also the case. These images were used to conclude that the loops form a family of Frank loop on the four {111} planes. The varient marked δ lies in the foil plane (111) and always appears by residual contrast.

$$p = \xi_g^w \text{ Cot}\theta \qquad \text{(see Fig. 4.3(a) and Table 4.1, Column 6)}$$

ξ_g^w is calculated from the formula

$$\xi_g^w = \xi_g^o / \frac{\xi_g^o}{\sqrt{1 + w^2}} \qquad \text{column 5}$$

where ξ_g^o silicon, g = 220, is 760Å

$$w = s\xi_g^o \qquad \text{column 4}$$

s = deviation parameter which is calculated as shown in Fig. 4.3 and listed in column 3

In Table 4.1 the measured fringe spacings are within ±10Å of those calculated assuming that $\theta = 70°$ i.e., that the loops lie on {111} planes. This is further justification that the loops lie on an inclined {111} plane.

The edges of the hexagonal defects lie along ⟨110⟩ and projected ⟨110⟩ directions (Fig. 4.2, Fig. 4.6(b)). Since only the {111} planes contain three coplanar ⟨110⟩ directions, this is also evidence that they lie on 111 planes. The sides of the loops lying on the foil δ plane (Fig. 4.6(b)) are equal, whereas, those on inclined planes have the inclined sides fore shortened. The ratio of the length of these sides reflect the angle through which the loops have been rotated. This angle was calculated for several loops and angles around 68° were found. This within 10% of the true 70° tilt assuming the loops lie on {111}.

Table 4.1. Fringe spacing as measured on the electron micrograph are shown in Column 7. These agree within experimental error (±10Å) with calculated values assuming that the loops lie on an inclined {111} plane shown in column 6.

1	2	3	4	5	6	7
Weak-Beam Reflecting Condition	Fig.	(sg)Å^{-1}	ω	ξg Å	Calculated Spacing Å	Measured Spacing Å
(g,2g)	4.1a	5.05×10^{-13}	3.83	190	69	70.5
(g,3g)	4.1c	1.14×10^{-3}	8.65	87	32	35
(g,4g)	4.1d	2.02×10^{-2}	15.3	49	18	20

Fig. 4.2. a. (g,2g), b. (g,2gs+), c. (g,3g), d. (g,3gs+), e,f. (g,4g). A series of weak-beam images (g,ng) where by tilting n is changed as above. Going from a to e the effective extinction distance decreases and the number of displacement fringes within the loops increases (c.f. loop A in Fig. 4.2a and 4.2e). The spacing between the fringes was used to calculate the inclination of the loop habit planes and it was confirmed that they were {111}. The edges of the defects (e.g., A) lie along ⟨110⟩ directions and is additional evidence that the loop habit plane is {111}.

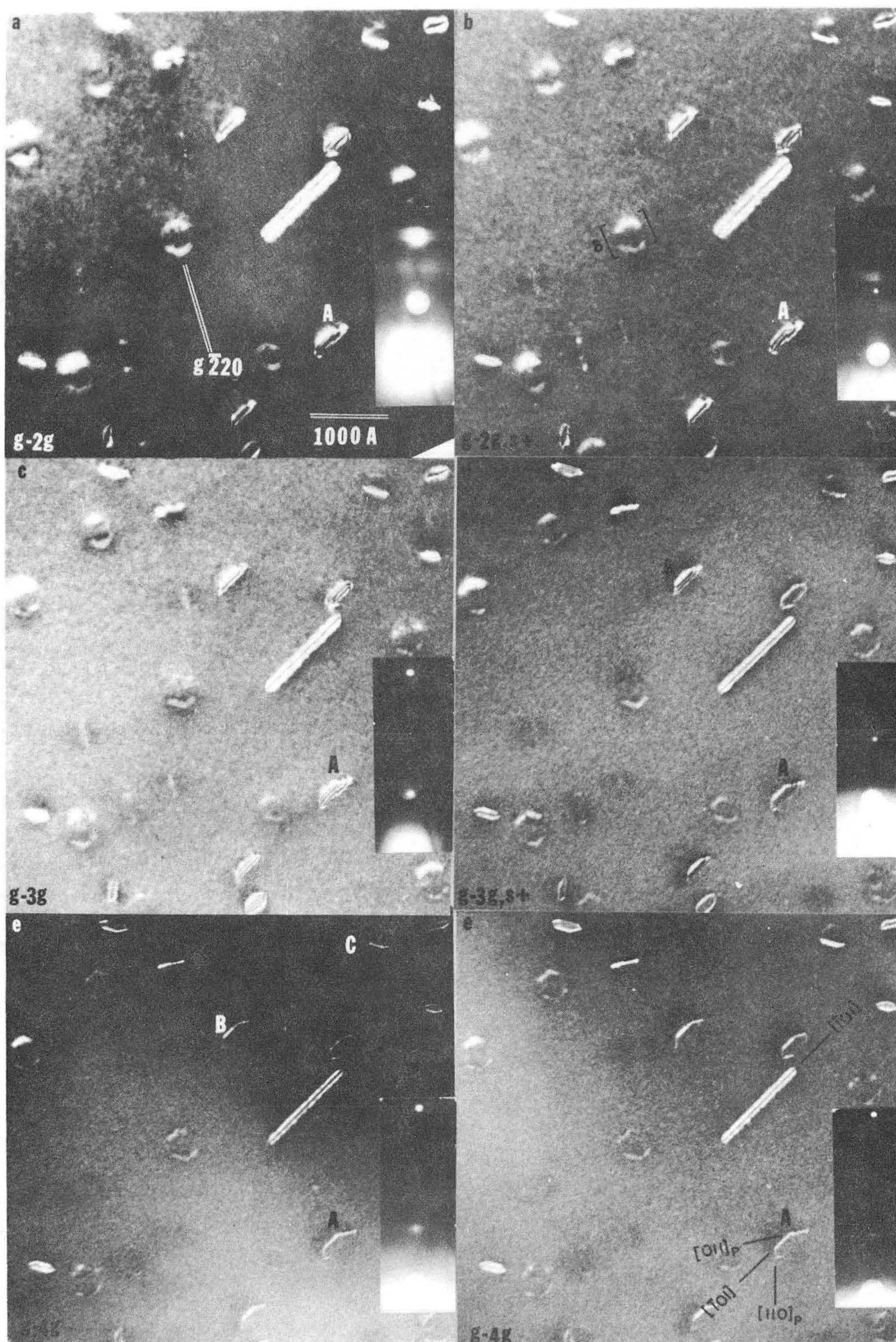

XBB 745-3357

Fig. 4.2

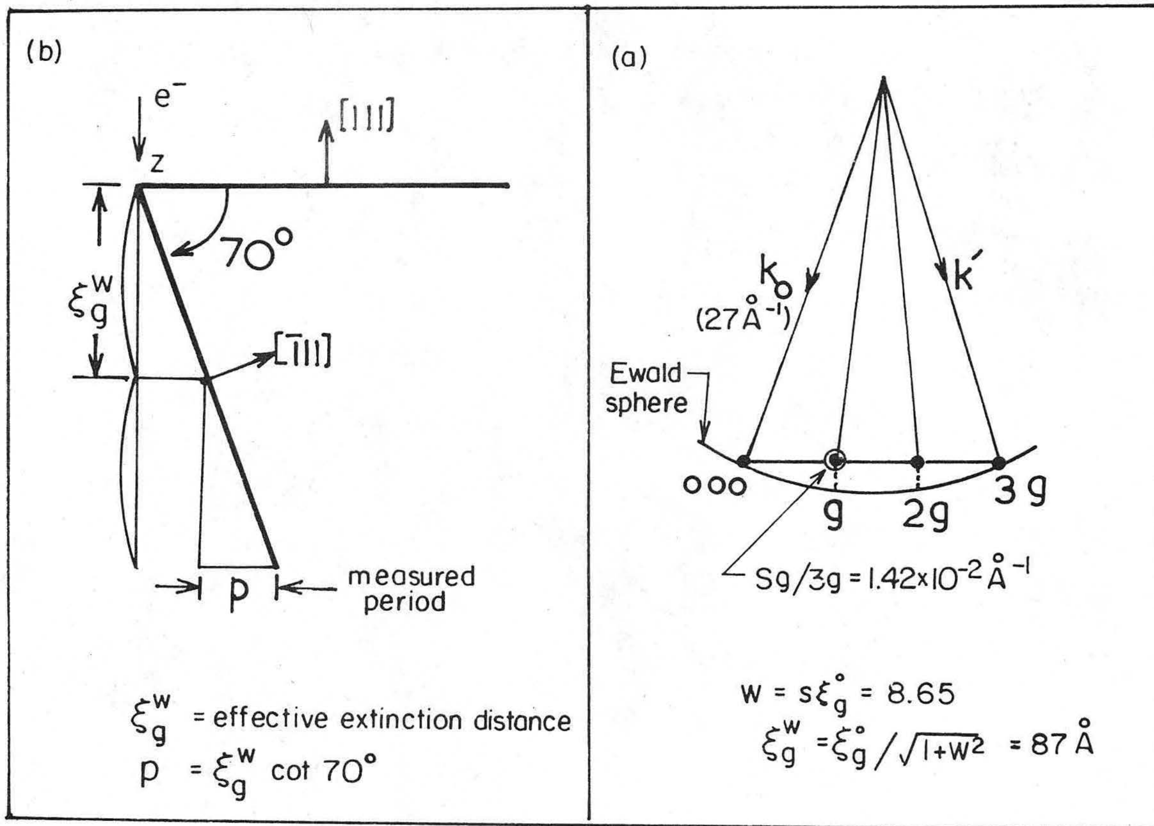

XBL 747-6675

Fig. 4.3. (a) Shows the reflection condition satisfied for the (g,3g) condition corresponding to Fig. 4.2c. The calculation of the deviation "s" for the reflection g, of w the dimensionless derivation and the effective extinction distance ξ_w^g is illustrated. (b) Illustration of how the value of the effective extinction ξ_w^g is used to calculate the fringe spacing. Notice that the fringe spacing depends on the angle the defect habit plane makes with the foil plane. This angle is 70° if the defects are assumed to be on {111} planes.

From the above it is concluded that the defect habit planes for the great majority of loops on the p-type foils examined were {111} and that they were Frank loops. In addition, there were a few unfaulted perfect loops as at A in Fig. 4.1 which show very dark interiors (see Section 4.2.3). Linear defects in densities of about $10^{15}/cm^3$ were also found. Loop densities are of the order of 10^{15}-$10^{14}/cm^3$ (Davidson, 1971; Madden, 1973).

4.2.2. Determination of Defect Type

Defects lying on the inclined 111 planes were first analyzed; they are easily imaged with reflections in the 111 zone. The loops in the foil plane were analyzed at the (112) pole using $g = 11\bar{1}$.

The stereo pair in Fig. 4.4 is used to find the loop type. These images demonstrate that it was impossible to determine loop habit from conventional images. That the habit is {111} was determined using weak beam images and described previously (Section 4.2.1). Accordingly in Fig. 4.4, the loops marked β showing outside contrast are expected to be on the 111-β plane and those marked γ and showing inside contrast on the 111-γ plane. The analysis of the strain contrast is shown in Fig. 4.5. Using the formal FSRH analysis (Hirsh et al., 1969) the β varient shows outside contrast requiring that $(g \cdot R_\beta)\ s < 0$. Since s is positive and g is fixed as shown, R_β must be as drawn in Fig. 4.5c, requiring that the loops are interstitial. The same is true of the γ varient. The same result is found if the rotation of the planes around the defect is examined (Fig. 4.5c). These analyses confirm that the loops in the inclined planes are interstitial Frank loops.

Loops in the foil plane (δ loops) are analyzed in Fig. 4.6. In Fig. 4.6a and δ loops appear by residual contrast. Using the specially

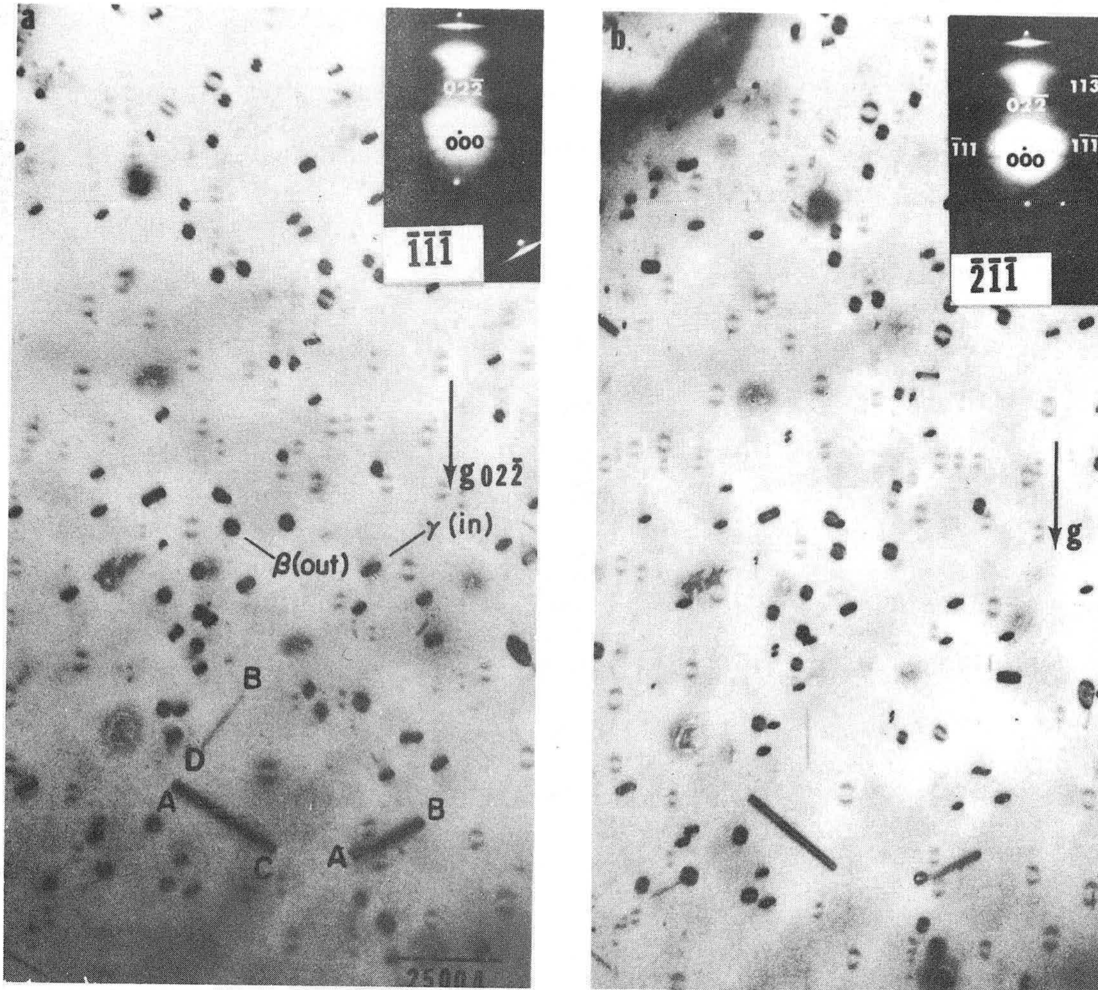

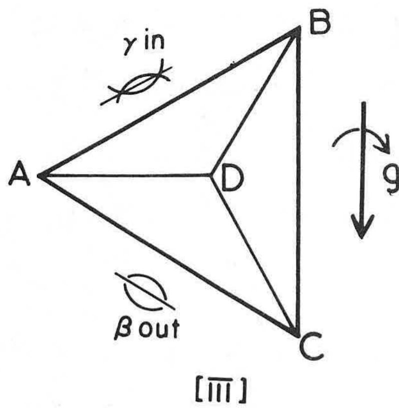

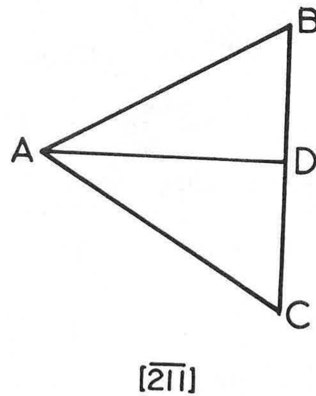

XBB 745-3334

Fig. 4.4. A bright field stereo-pair where (a) is near 111 and (b) is near 211. Notice that the B varient shows outside ($g,R_B<0$) and the γ varient inside ($g,R_B>0$) contrast. "S" the deviation is positive for both images shown in the diffraction pattern.

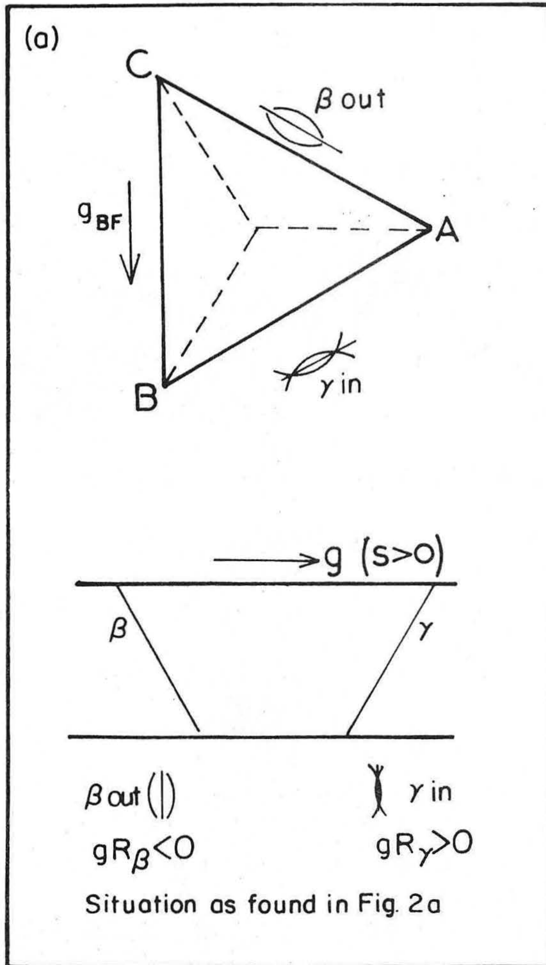

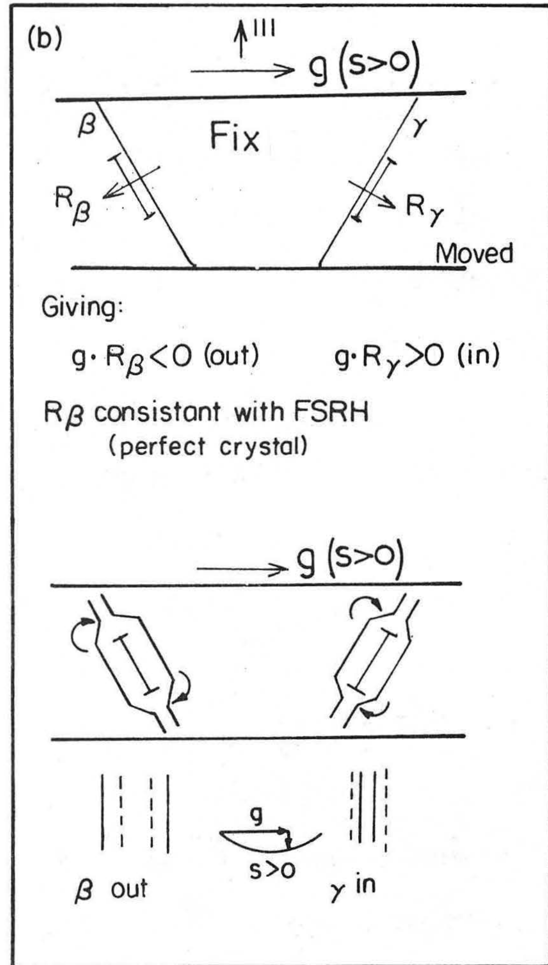

XBL 745-6241

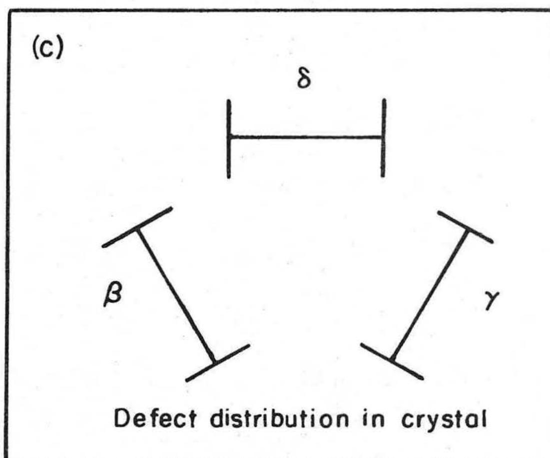

Fig. 4.5. Analysis of the loop type in Fig. 4.4. (a) Shows the inclinations of the B and γ planes in top and side view with the information obtained from Fig. 4.4. (b) Shows the analysis in terms of the FSRH convention. If the top of the crystal is fixed, $R_β$, and $R_γ$ must be as shown. The analysis is repeated taking the bending of the planes into account. The result is that the loops are interstitial. (c) Shows the distribution of interstitial defects on the four {111} planes.

constructed wedge, the foil was tilted to the [112] pole where the δ loops appear as grey regular hexagonal discs. They appear in strong contrast in Fig. 4.6b and weak contrast in Fig. 4.6c. This special feature is discussed in detail in the next section. At C, D and E some perfect loops showing very dark inside contrast appear.

The determination of loop type is shown in Fig. 4.7. The inside contrast in Fig. 4.4b requires that $(g\cdot R\delta)\ s > 0$. Since $\hat{g}$ is fixed and s is positive as shown, $R\delta$ must be as shown in Fig. 4.7e; consequently the loops are interstitial. Analysis of the rotation of the planes yields the same result; it was concluded that the loops on the foil plane were also interstitial.

This conclusion is strongly corroborated by the interesting reaction between a loop on the [111] foil plane and one on an inclined (111) plane at E. Since the two stacking faults meet at 120° and the other two Frank dislocations appear to have attracted one another the two loops participating in the reaction are of the smae type viz interstitial.

One researcher found vacancy loops in the foil plane upon annealing P^+ ion damage. This would imply that stress plays a major role in the type of loop nucleated on a given habit plane. It should also lead to a preferential distribution of a given set of loops within a depth range where the internal stress favors their nucleation. No evidence for this effect was observed in the present experiments.

Stereo measurements which indicate that there is no depth segregation of loops by habit plane or type, are presented in the following section. The loops in the foil plane are well distributed among those

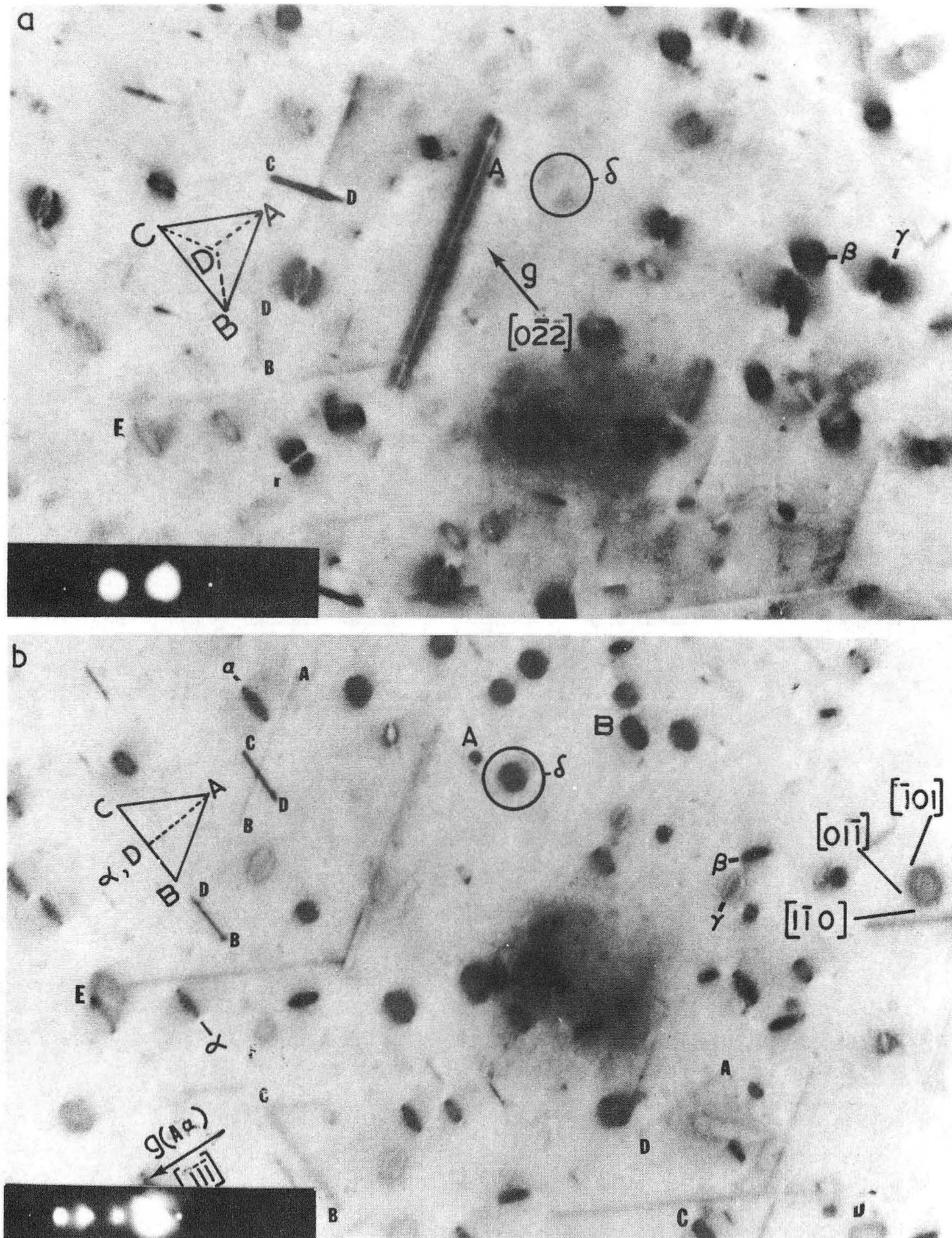

XBB 747-4423

Fig. 4.6. (a) Shows a bright-field image at the 111 pole where the loops in the foil plane (δ) are in residual contrast; the other varients present (B,γ) are indicated. (b) Shows the same area at the 211 pole using g = $1\bar{1}\bar{1}$. The loops in the foil plane δ are visible and show strong inside contrast. They are hexagonal with sides along ⟨110⟩ directions. Linear defects along the various ⟨110⟩ directions are marked. Loops B, C and D are perfect loops and show very dark inside contrast.

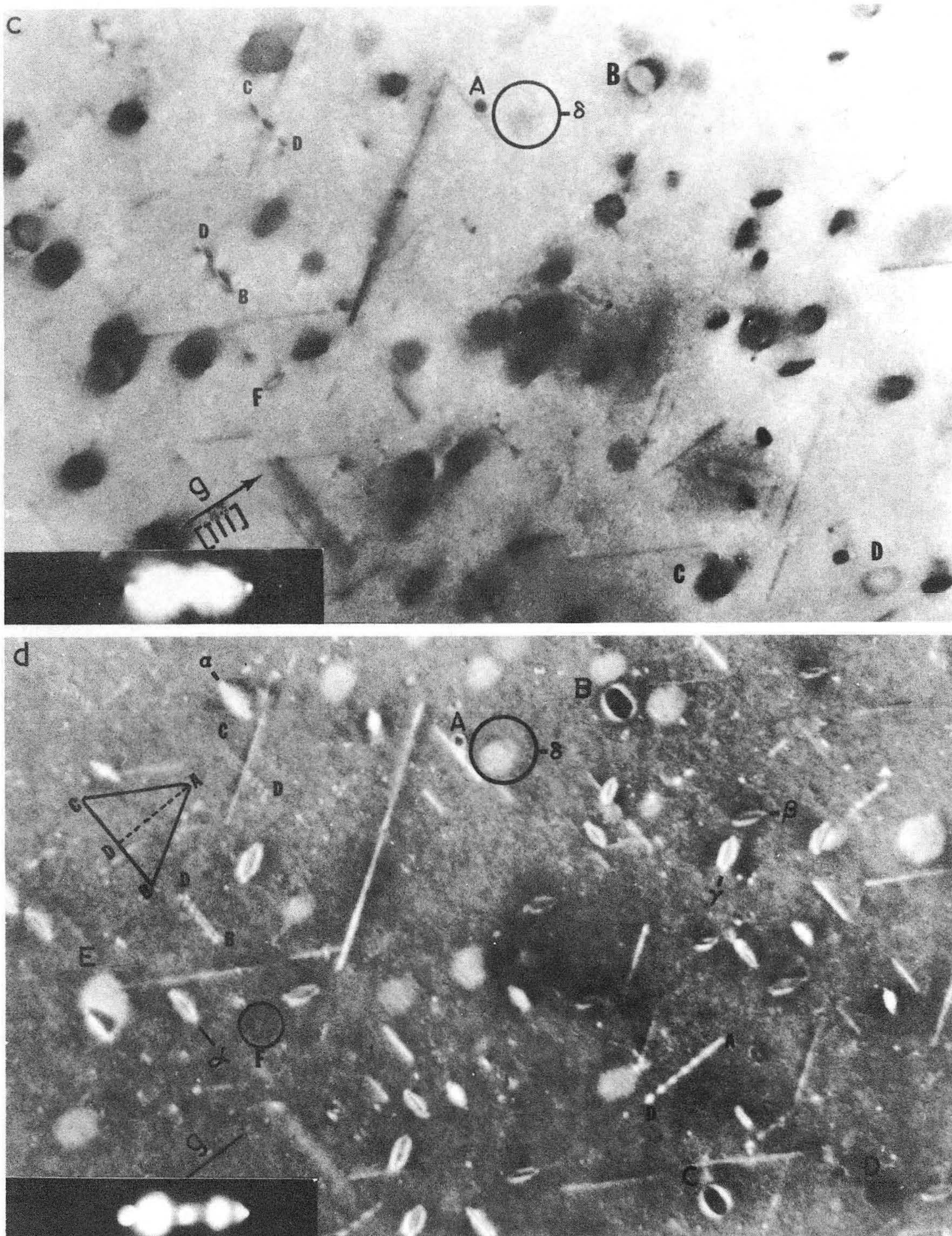

XBB 747-4424

Fig. 4.6. (c) The same area in g = $\bar{1}11$. The δ loops now show very weak outside contrast. It was checked that this effect depends only on the sign of (g·s) s. (d) The same area in (-g,2gs+) weak-beam. The various sets of defects are marked according to the Thomson tetrahedron. The perfect loops A, B and C show very dark interiors. At E is a reaction between a loop on the δ plane and one on the inclined α plane.

Fig. 4.7. Analysis of loops in the foil plane d. (a) Shows the crystal in top view. The poles shown are projections below the crystal. (b) The same crystal tilted to the $\bar{2}\bar{1}\bar{1}$ pole (as in Fig. 4.6b). The vectors $\hat{n}$, the foil normal, $\hat{g}$ and the sign of s pertaining to Fig. 4.6b are shown. (c) The δ loops in Fig. 4.6b show inside contrast requiring that $gR\delta>0$. Therefore, the direction of $R\delta$ should be as shown in Fig. (c). The loops in the foil plane are therefore interstitial. (d) The analysis taking the rotation of the planes into account giving the result that the (δ) loops are interstitial.

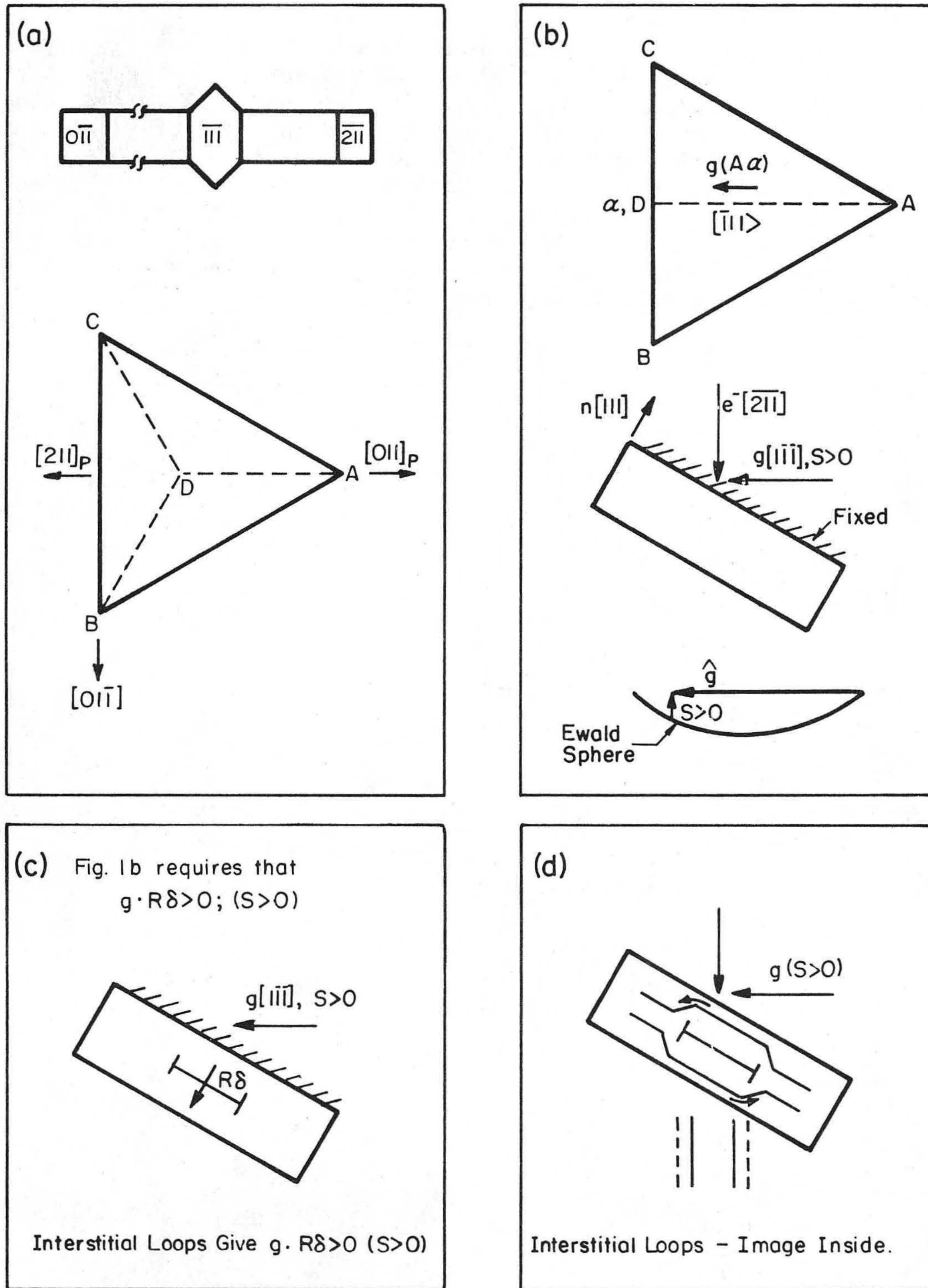

XBL 745-6413

Fig. 4.7.

on inclined planes. This indicates that stress aided or stress inhibited nucleation is not an important factor in the annealing process despite the large internal stresses (2×10^{19} dynes/cm^2) that have been reported (Ernisse, 1969).

The special contrast effects, namely the great change in outside to inside contrast in Frank loops (Fig. 4.6b,c) and the dark interiors of perfect loops (Fig. 4.6b at B for instance) are discussed in the next section. There it is concluded that this could indicate dopant atom segregation to the stacking fault. This could result in a small change in the displacement vector of the Frank loops from $a/3\langle111\rangle$ to $a/x\langle111\rangle$ $x > 3$ and that of the perfect loops from $a/2[110]$ to $a/2[110]-a/y[111]$. This is discussed in more detail in Chapter V.

4.2.3. Contrast Effects-Depth Distribution

It was mentioned in Section 4.2.2 that the perfect loops showed very dark inside contrast and weak outside contrast (see Fig. 4.1). This has been previously noted by Davidson and Booker (1971) who were the first to ascribe it to precipitation at or near the loop. They did not suggest any mechanism by which this may occur, however. This effect is also seen in some recent images (Bicknell, 1973); this author does not draw any specific inference from the effect.

In this study, the perfect loops as well as the Frank loops showed the contrast effect mentioned above, both in bright field (Fig. 4.8) and in weak beam (Fig. 4.9). In Fig. 4.8a the foil was imaged at the 111 pole with $\hat{g} = 02\bar{2}$ so that the loops in the foil plane ($R\delta = 111$) are not visible except by residual contrast ($\hat{g}\cdot R\delta = 0$). In Fig. 4.8b and c they are imaged with g + and - $\bar{1}\bar{1}\bar{1}$ at the [112] pole. The great

difference in inside and outside contrast is obvious. The same is true for the weak-beam images (Fig. 4.9). For instance, Frank loops formed by quenching pure aluminum (Eddington and Smallman, 1965) and examined with g = tor - [111] do not show this great change in contrast. Frank loops formed by quenching pure aluminum (Eddington and Smallman, 1965) and examined with ±g = 111 do not show this change in contrast.

One possibility is that this is a depth related effect: that the defects at a certain depth show dark contrast while those at another show weak contrast. In order to check if this was so, the depth in the foil of several loops in the foil plane and of those on inclined planes were determined by stereomicroscopy and subsequent parallax measurement. The results are shown in Fig. 4.10. The loops in the foil plane lie well distributed within a depth of 1500Å. Since most of the loops in the field of view show the effect, this is probably not a depth effect but a property of the defects themselves.

Another explanation is that the uniform contrast occurs by the overlap of dislocation tails (Low and Turqualo, 1968).* However, such an overlap should not depend upon the sign of $(\tilde{g}\cdot\tilde{b})$ s. Since the contrast from these defects do, this explanation is perhaps not adequate.

The similar contrast effects observed in the Frank loops and described in Section 4.2.3 is, therefore, interpreted as structure factor contrast arising from impurities adsorbed on the stacking fault. The contrast effect observed in the perfect loops could then be explained on the basis that the adsorbed atoms remain after the loop has unfaulted.

---

*I am grateful to Dr. M. J. Goringe for this suggestion.

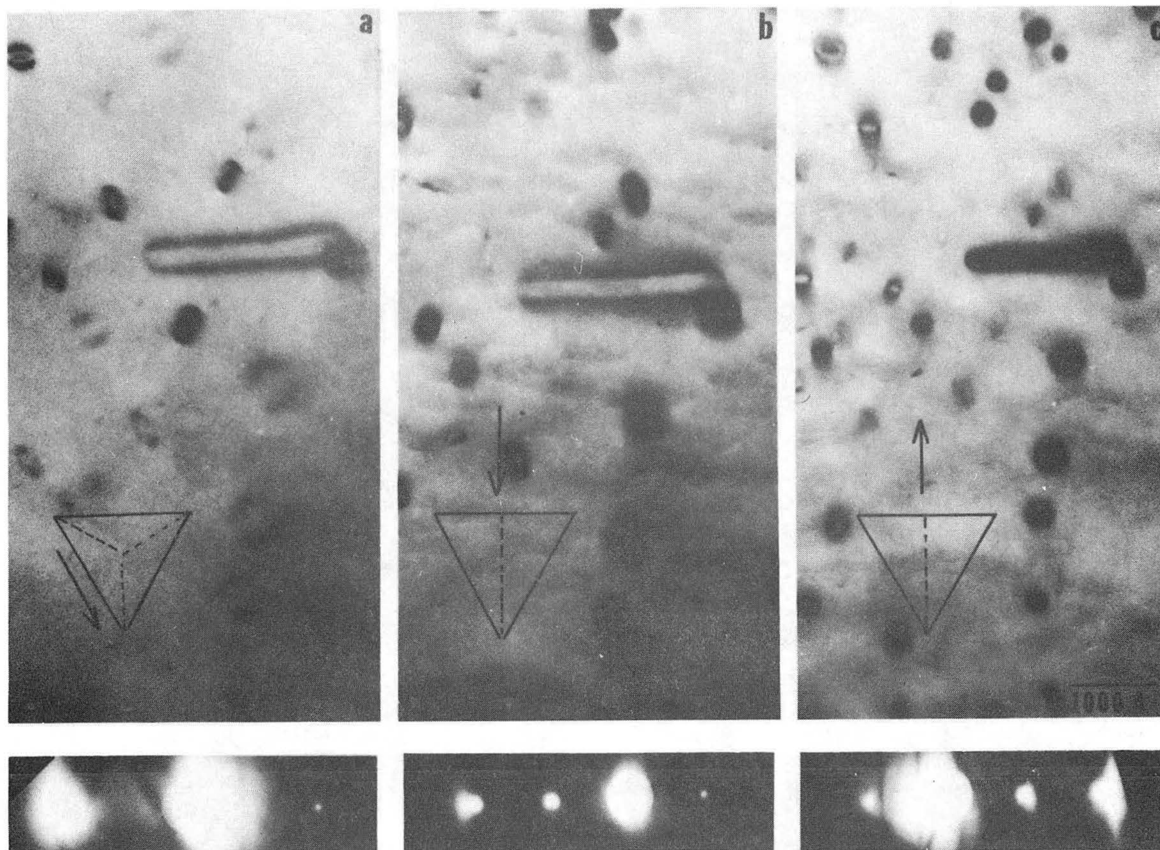

XBB 7410-7194

Fig. 4.8. To show the great difference between inside and outside contrast shown by loops. (a) Shows the loops in residual contrast, (b) shows the loops in weak outside contrast and (c) shows the loops in strong inside contrast. This is not a depth effect (see text); it could arise from the segregation of impurity to the loops.

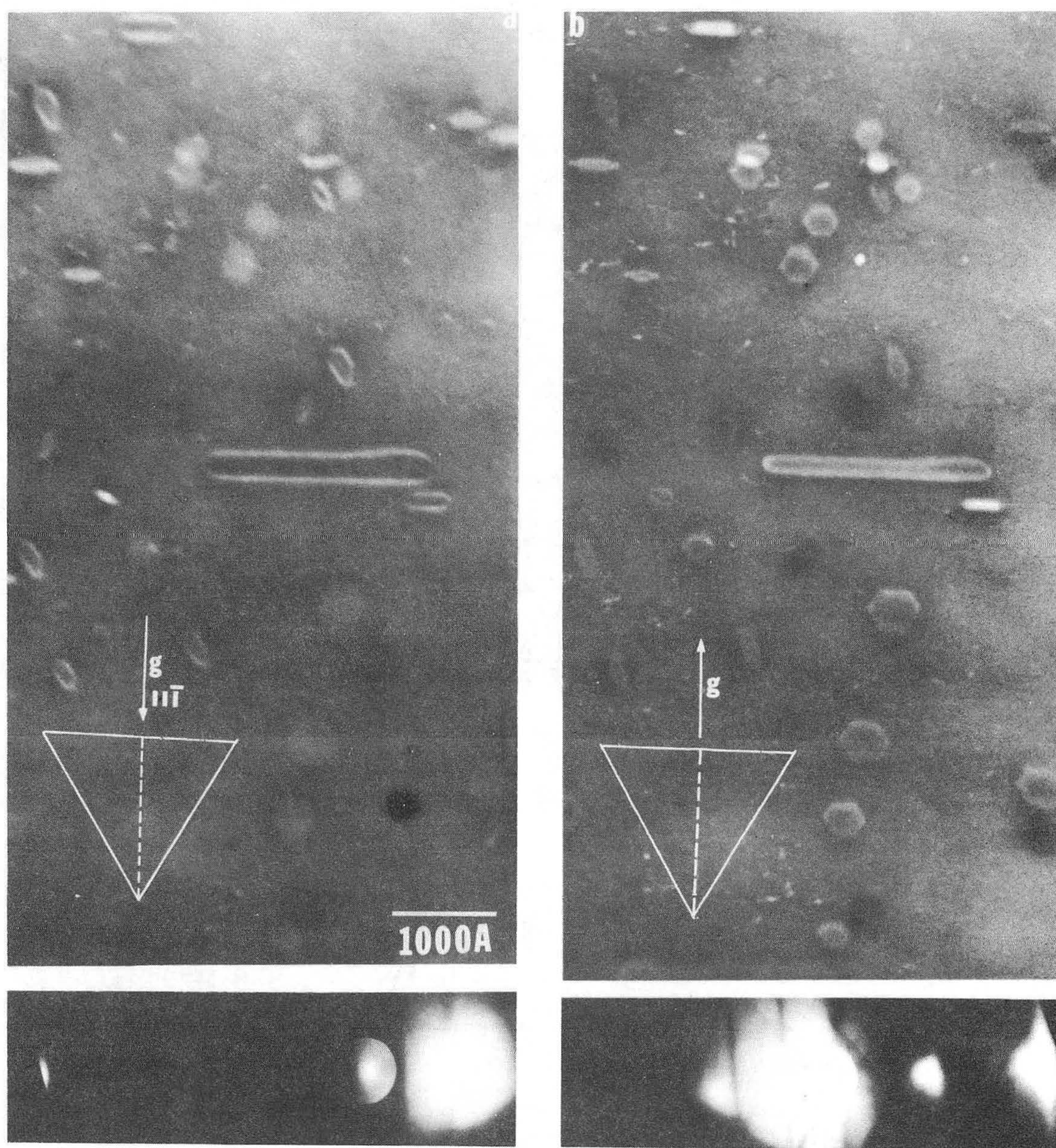

XBB 7410-7195

Fig. 4.9. The same images in ±g in two weak beam conditions: (a) (g,4gs+) (b) (-g,-3gs+). The loops show faint outside contrast in (a) and strong inside contrast in (b). The effect does not depend on "s" but only on the sign of (g·b) s.

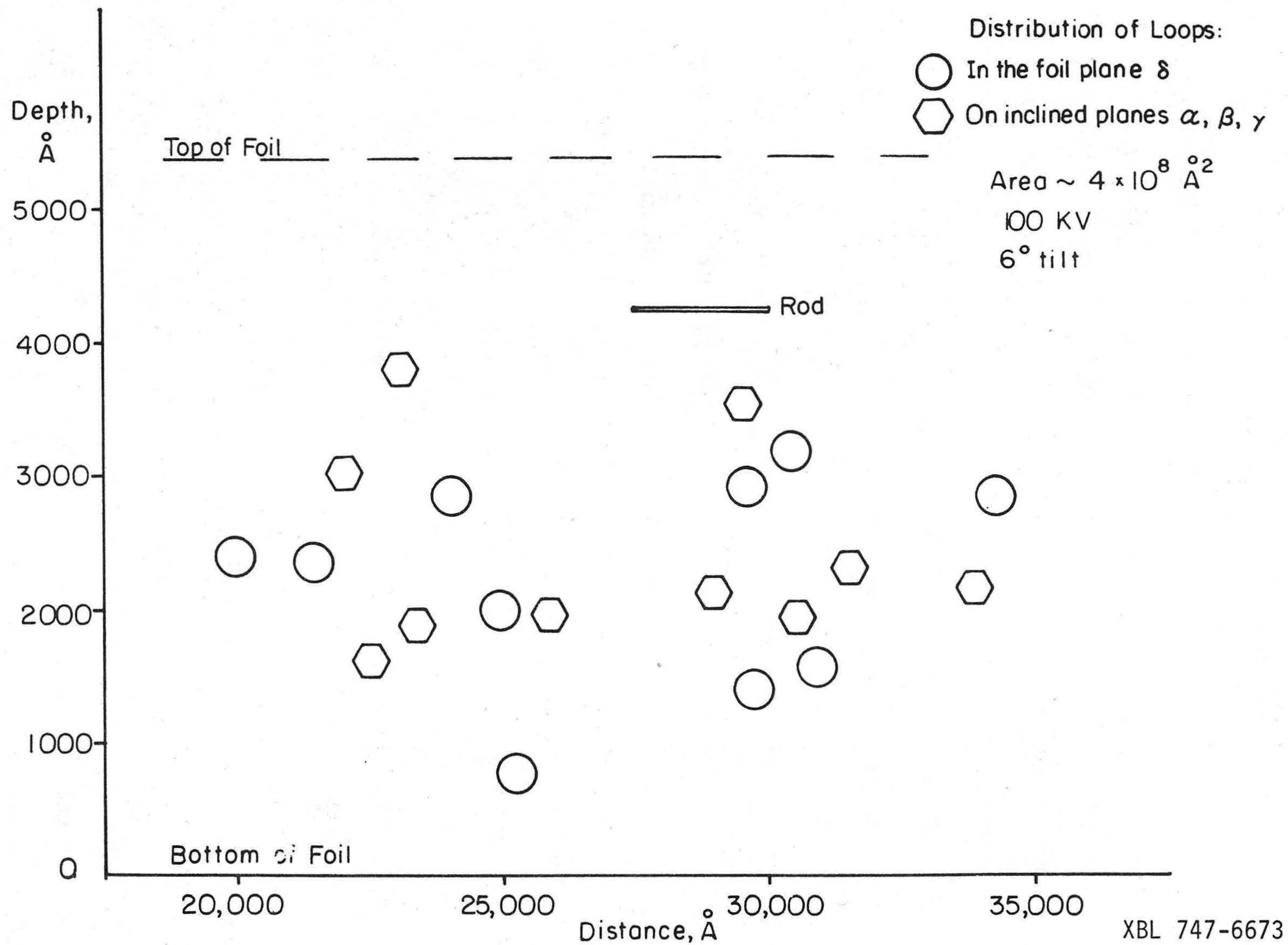

Fig. 4.10. Distribution of loops in the foil plane compared with the distribution of those on inclined planes. The δ loops are uniformly distributed over a depth of about 3000Å.

4.3. Defect Morphology-Silicon Prehistory

Descriptions of defect morphology for annealed P^+ ion implanted silicon are varied as is explained in Section 4.1; the origin of this variation is not clear. In order to investigate whether the presence of piror dopants in silicon alter the defect morphology P^+ ions were implanted into

a. n type (phosphorous doped) 111 silicon

b. n type (phosphorous doped) "lopex" (low oxygen) 111 silicon

c,d. n type (antimony doped) 111 silicon

(The letters correspond to Fig. 4.11.)

In addition, two p (boron) doped silicon wafers, one implanted with P^+ and the other with SiH^+ ions were examined. The substrates were all about 1 Ωcm and the dose was 2×10^{14} ions/cm^2 in all cases.

The defects formed in P^+ and Si^+ implants were not very different from each other. Frank loops and linear defects were observed. Fewer defects were observed in the SiH^+ implants. A possible explanation is that damage is sensitive to size of the implanted ion.

Defects observed after annealing the n-type foils were different from those in the p (type) foils and from each other as shown in Fig. 4.11. The fraction of larger and more circular loops was greater in n type fails. These were examined at the ($\hat{g}$,3$\hat{g}$) weak beam condition and showed no fringes indicating that they were perfect. Also, no linear defects were observed. Figure 4.11c and d shows that these loops also show very strong inside contrast (e.g., at A in Fig. 4.10c) and weak outside contrast, e.g., Fig. 4.11d, suggesting some precipitation (Davidson and Booker, 1971).

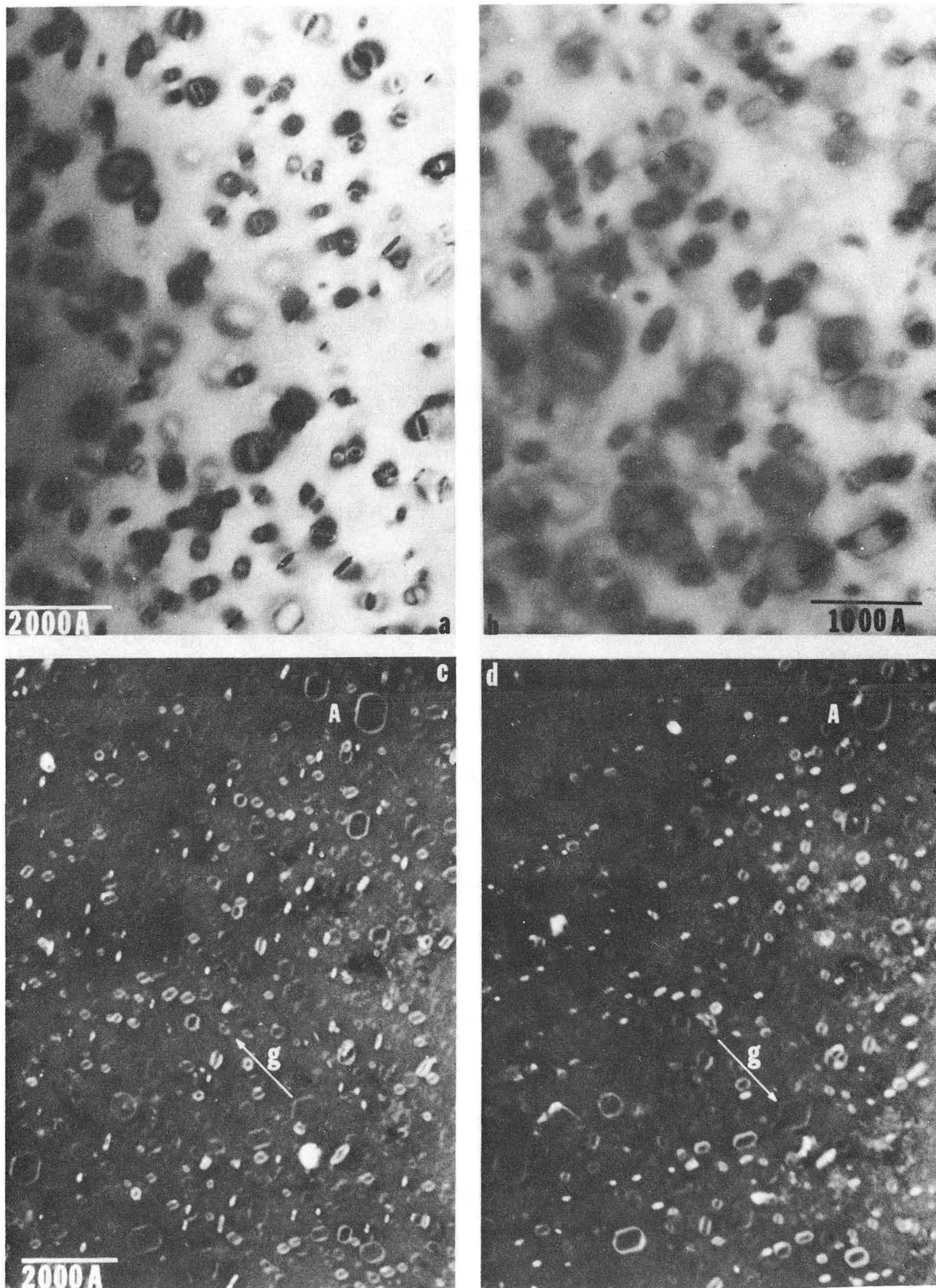

XBB 7410-7190

Fig. 4.11. A comparison of loop morphology when the dopants in the substrate are changed. Shown are (a) n(P) Si, (b) n(P) lopex Si (c,d) n(sb) Si all implanted with P^+ ions (2×10^{14} i/cm^2) and annealed to 800°C for 2 min. Linear defects are not formed. The loops are larger, circular and mostly perfect.

The possibility that dopants may be adsorbed on the stacking fault provides a simple explanation not only for the contrast effects observed but also for the relatively poor electrical activity of foils containing such Frank loops reported by Crowder and Moreheat (1969).

These ideas are further developed in Chapter V.

It was concluded from this experiment that defect morphology resulting from phosphorous implantation and annealing is sensitive to the presence of solutes. The presence of larger dopant atoms phosphorous and antimony, favored the growth of perfect loops. A possibility is that the higher internal stress, associated with atoms of larger misfit, promotes nucleation of perfect loops or unfaulting of Frank loops.*

Since linear defects were only observed in foils containing boron (e.g., B^+ implanted foils and P^+ implants in boron doped foils) and absent when no boron was present (e.g., in n (P doped) and n(sb doped) foils as above), it was concluded that boron is necessary for growth of linear defects.

The annealing behavior and depth distribution of linear defects is described in the next section.

---

*I am grateful to Dr. Westmecott for this suggestion.

4.4. On the Presence of Linear Defects

Chadderton and Eisen (1971) showed that for room temperature B^+ implantation "rod-like" linear defects were formed along the [110] directions. These foils showed an increase of electrical activity which coincided with the disappearance of the rods. It was concluded that B was associated with these defects.

Bicknell (1973) reports that linear defects were absent in P^+ implants. This was correlated with the absence of any abnormal increase in the carrier concentration vs annealing temperature curve implying that P^+ dopants do not form linear defects. In contradiction to this linear defects were found in P^+ implants used in this study (Seshan and Washburn, 1972). Tamura and Ikeda (1972) reported linear defects in high temperature P^+ implants (1974). More recently, Madden (1973 has reported the presence of linear defects in P^+ implants at room temperature.

The experiments described below were done to study the linear defects in more detail. In Fig. 4.12 a foil is shown which was partly masked from the ion beam, annealed at 800°C and then examined. Loops and linear defects formed only in irradiated areas. This experiment eliminates the possibility of contamination from the furnace atmosphere; the defects are associated with the damage process. Similarly, foils were heat treated in different furnace atmospheres e.g., a 4% H_2-96% He mixture, and in extra pure helium and the specimen cooling rate was changed; wafers of 111 and 100 were also used. Linear defects were found in all p-type foils regardless of orientation and heating procedure. It was also confirmed by examining epi on epi wafers that the mechanical polishing of silicon prior to implantation does not affect linear defect formation.

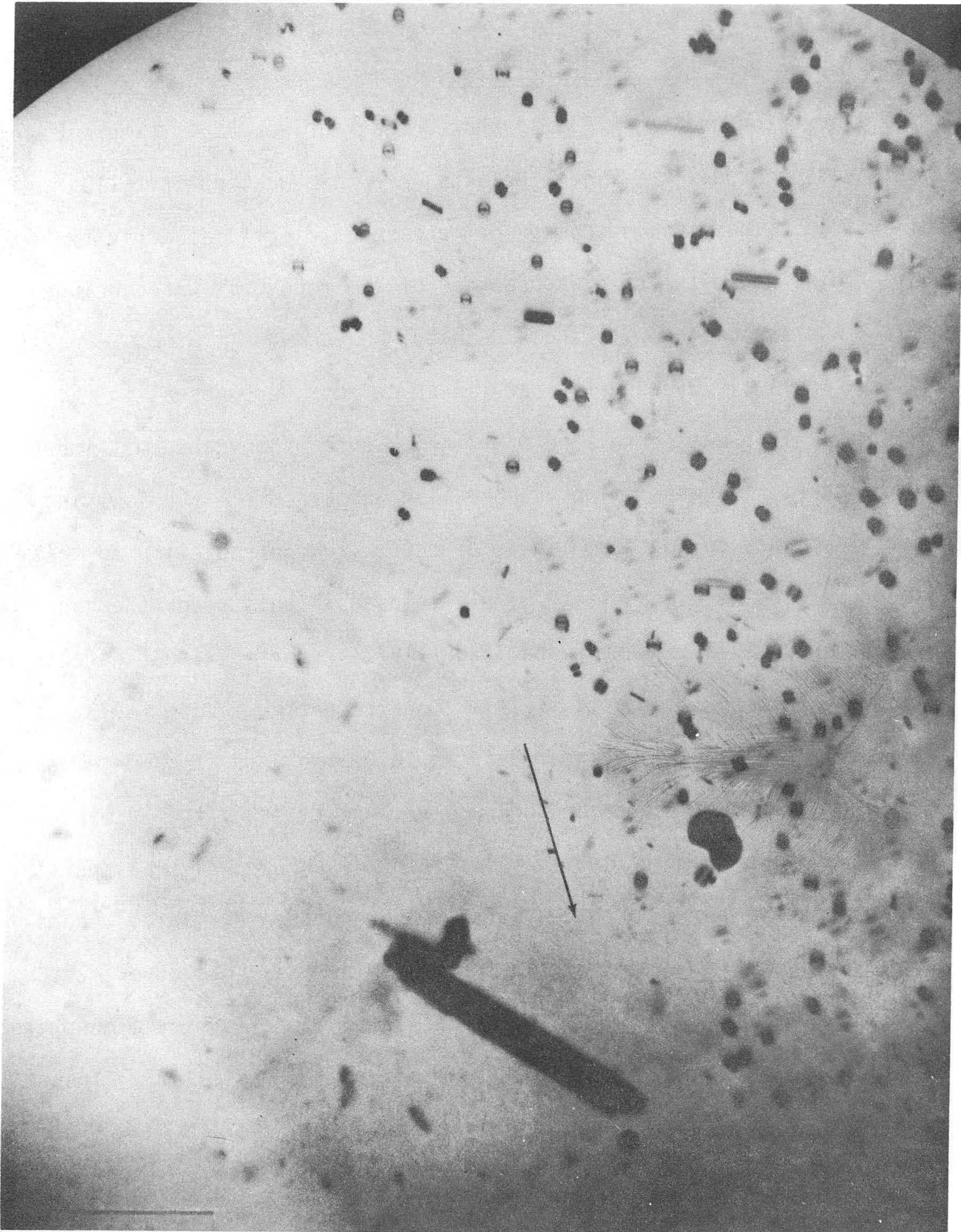

XBB 744-2291

Fig. 4.12. Shows an area partially exposed to the ion-beam. Subsequent annealing shows that no defects form in the areas not bombarded. The possibility that furnace contaminents affect defects is eliminated.

Linear defects were observed only in foils containing boron (Section 4.3). It was, therefore, concluded that boron was necessary for the linear defects to form (Seshan and Washburn, 1975).

The result that linear defects are formed in hot implants (Tamura, 1971) is interesting in that it suggests that foil heating is important. The claculation in Chapter II shows that beam heating can be a problem if a good heat sink is not provided. The temperature rise of the foils examined in this study was not expected to be over 50° (Reddi, 1974). However, foils implanted using different types of heat sinks were not examined.

In order to study the annealing behavior, depth distribution data was obtained for rods and loops using stereomicroscopy. Foils were tilted 6° along the g = 220 Kikuchi band and images under identical diffracting conditions were obtained. Parallax measurements were made using a Wilde parallax bar and sterescope. The depth distribution of defects in a foil annealed at 800°C for 1/2 hr is seen in Fig. 4.13. No defects are seen within 1000Å from the implanted surface. (This is marked "top of foil" in Fig. 4.13.) This is consistant with theory that the incoming ions cause no damage for the first 1000Å where they suffer electronic collisions. The defects loops and linear defects are then distributed in a 3000Å deep layer where the ions suffer nuclear collisions, and come to rest, causing severe lattice damage.

The inclined rods along the three inclined [110] directions extend (from the layer of the loops) to the implanted surface. Depth distribution in another foil heated at 650°C for 2 hr is shown in Fig. 4.14.

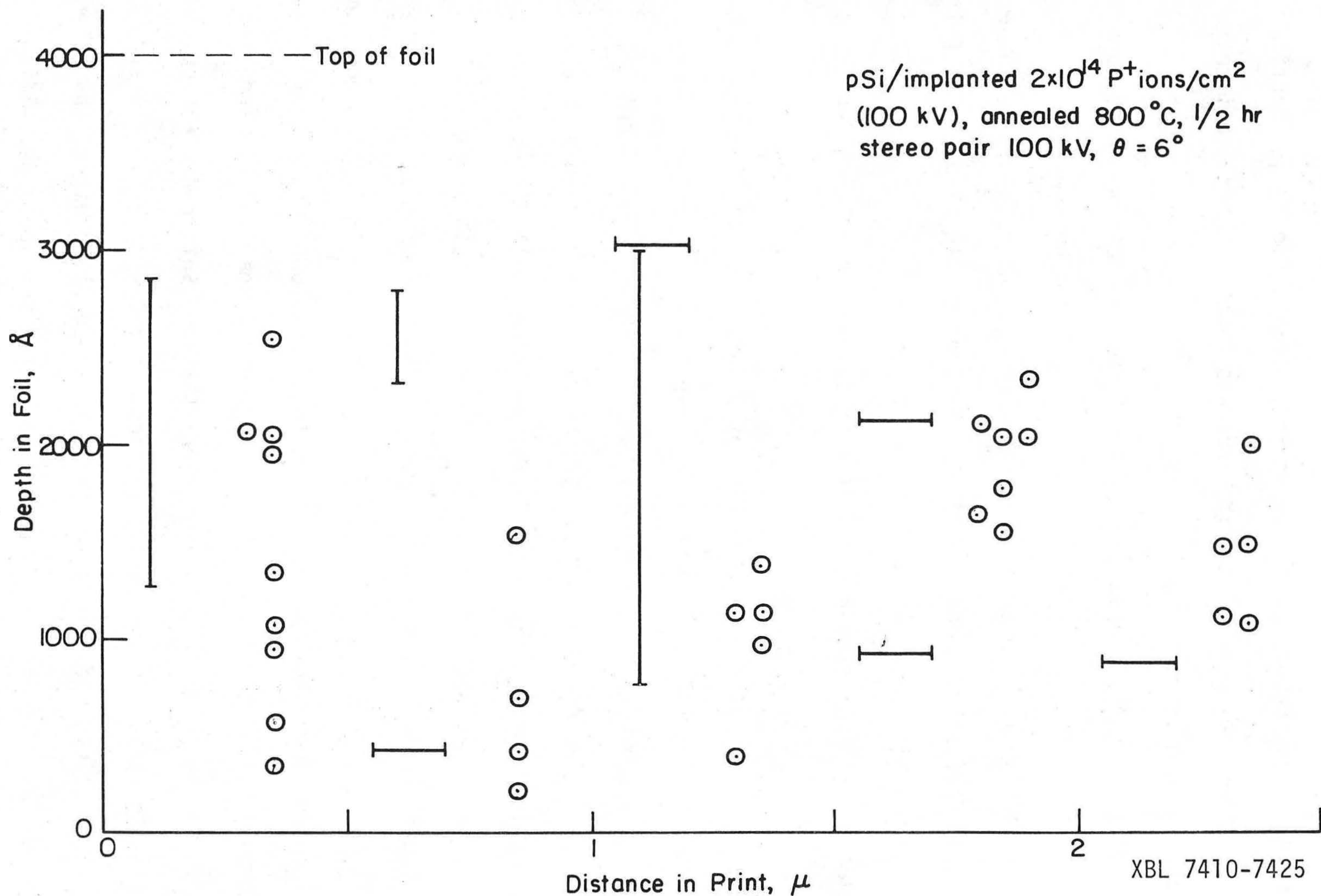

Fig. 4.13. A stereo-microscopic depth determination of linear defects and loops in a foil annealed at 800°C for 1/2 hr. The defects inclined to the foil surface (drawn vertically in this diagram) are longer than those in the foil plane.

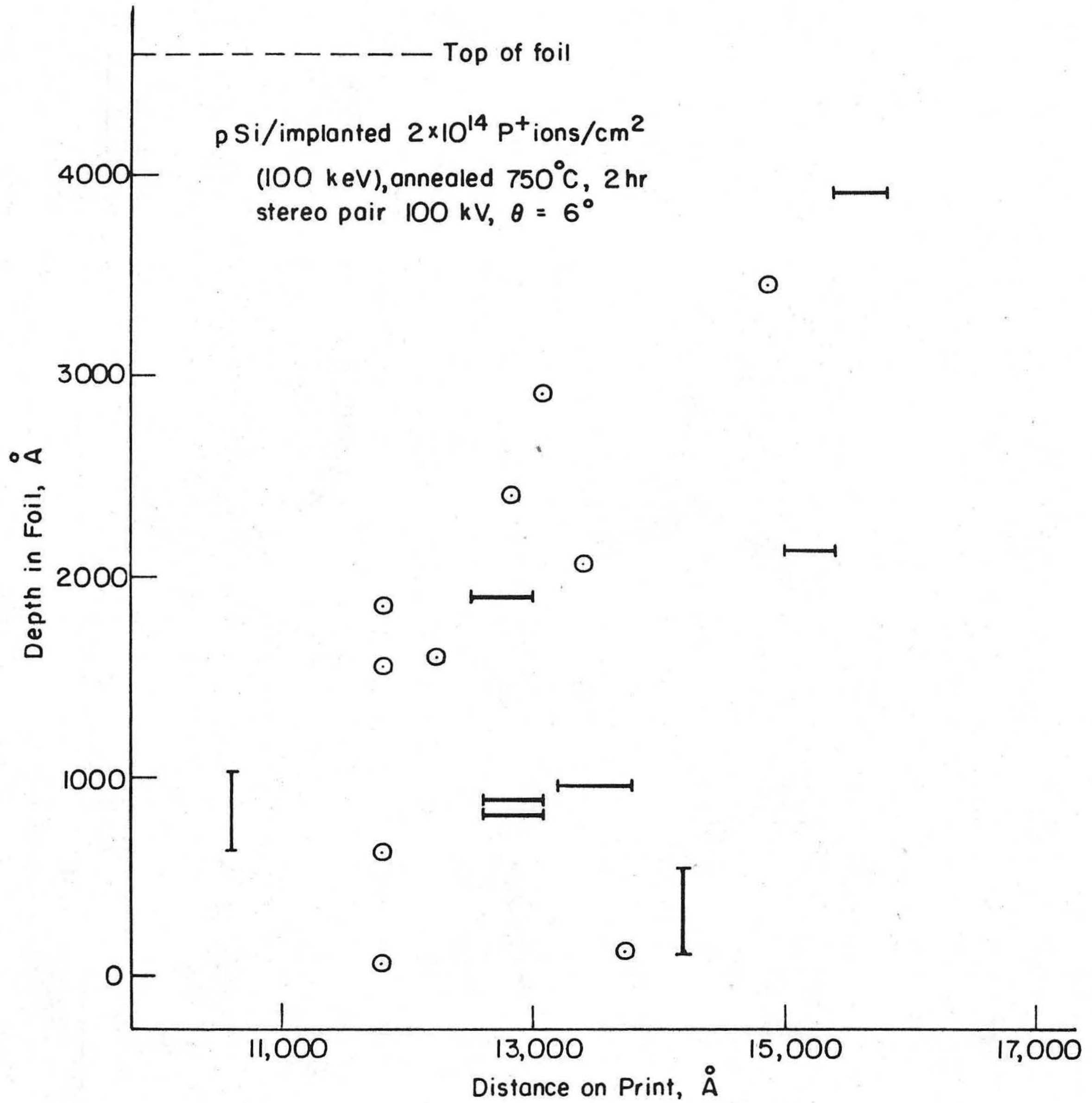

Fig. 4.14. Depth distribution of linear defects and loops in a foil annealed for a longer time than in Fig. 4.13. The linear defects inclined to the foil surface appear greatly reduced in length. The shrink by point defect emission to the top surface.

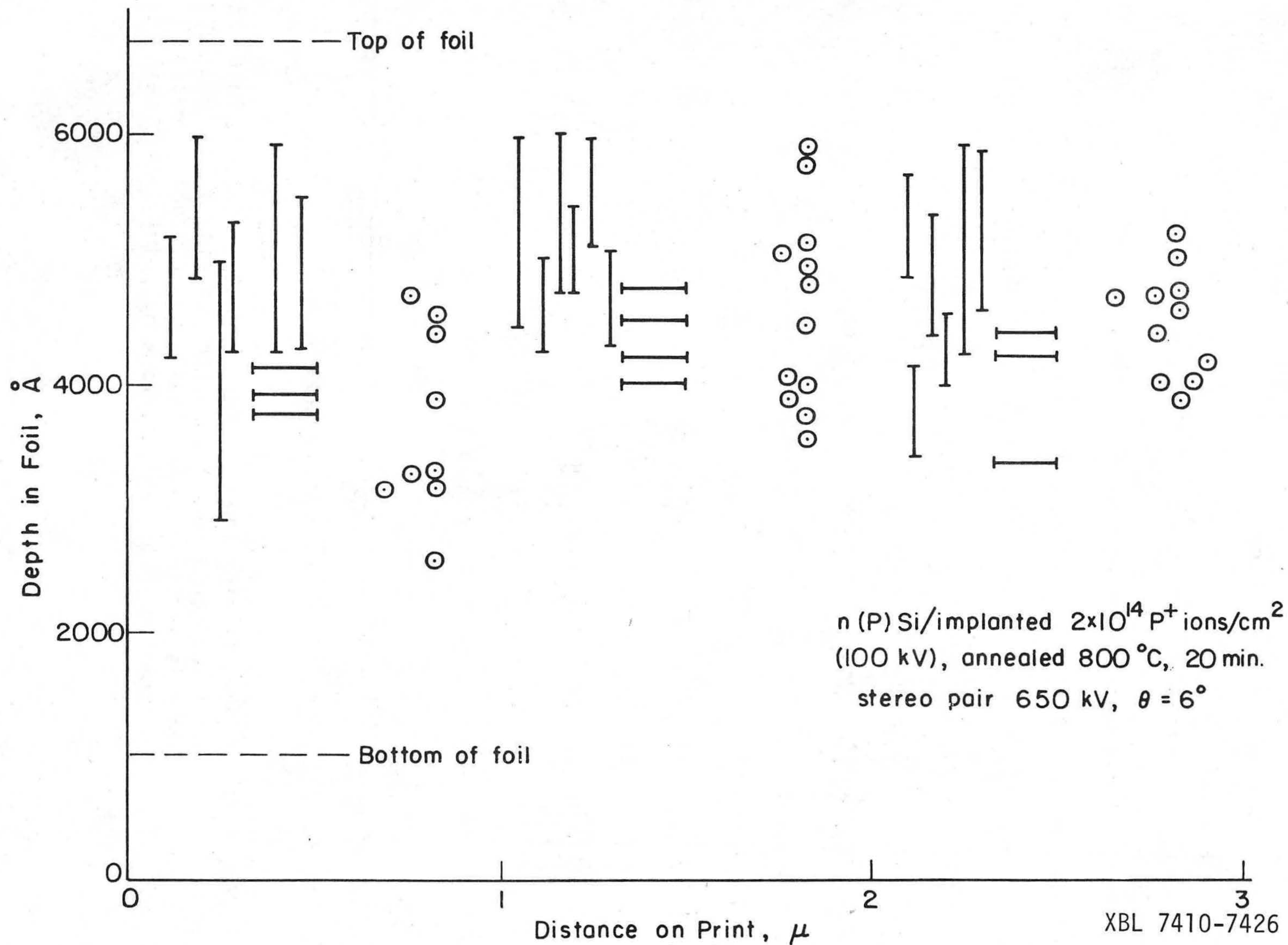

Fig. 4.15. Stereo depth distribution as determined in the high voltage electron microscope. The loops and the linear defects parallel to the foil surface lie distributed roughly over the same depth. The inclined defects extend from the layer of the loops to the top surface. There are no interactions between the rods and loops suggesting they are both interstitial.

Notice that the inclined linear defects have shrunk back from the end near the top surface. This suggests that they shrink by the emission of point defects to the free surface.

The advantage afforded by the greater penetration of the 650 kV electron microscope is illustrated by Fig. 4.15. The loops and the horizontal defects are distributed in the same depth region whereas most of the inclined rods extended to the top surface. It is also significant that the loops and the linear defects do not often interact. They probably compete for the same point defects and hence avoid each other during nucleation and growth. The linear defects must then be interstitial. This is also the conclusion of Madden and Davidson (1973) based on contrast analysis.

4.5. Discussion and Conclusions

For ion implantation doses where a continuous amorphous layer is not formed, defects in p-type P^+ ion implanted silicon are hexagonal interstitial Frank loops. Interstitial linear defects and a few perfect loops are also found. In n-type foils linear defects are not formed indicating that boron is necessary for their formation. The morphology of the loops depends upon the dopant atoms present in the s-licon prior to implantation. The loops also show contrast effects indicative of precipitation within the loop. It is, therefore, likely that the dopant atoms interact with the defects--including adsorption on the stacking fault within the Frank loops. This interaction may explain the contrast effects shown by perfect loops and is also an alternative explanation for the electrical inactivity of P^+ ions in these foils (Chapter V).

CHAPTER V.
A MODEL FOR THE PRESENCE OF INTERSTITIAL DEFECTS

5.1. Introduction 74

5.2. Model 77

5.3. Applications of the Model 91

"Absence of evidence is not evidence for absence." Anon

5.1. Introduction

Measurements of resistivity and carrier concentration in isochronally annealed non-implanted silicon shows that there is a rapid recovery of electrical conductivity in the 550-600°C range (Bicknel and Allen, 1971; Davidson and Booker, 1971). Infrared absorption (Vook and Stein, 1970; Cheng et al., 1966) and EPR studies irradiated silicon (Watkins, 1965) shows that vacancies are formed and are mobile at room temperature. Upon heating they anneal out at about 300°C. At this temperature there is a large increase in the numbers of divacancies and vacancy dopant complexes. These annealed out in the 500-600°C range. From a consideration of such studies, the presently held view of the annealing process is as follows:

a. At or below room temperature motion of vacancies control the formation of damage clusters (Vook and Stein, 1970).

b. Upon heating in the 300-400°C range these initial damage clusters anneal by the liberation of vacancies; these then coalasce to form divacancies and more stable vacancy dopant complexes (Mayer, 1971).

c. Upon heating to 400-600°C the divacancies and vacancy-dopant complexes "anneal out"; dopant atoms become substitutional and hence electrically active (Bicknell, 1971). However, in the case of P^+ implants in the 10^{14} ions/cm^2 range, only 30% of the implanted atoms are electrically active after a 600°C anneal (Crowder and Morehead, 1969).

d. electrical inactivity of the dopants in the early stages occurs by vacancy compensation (Vook and Stein, 1970).

The above explanation besides ignoring the role of the interstitial, gives no suggestion as to what happens to the divacancies when they anneal out. In Chapter I it was pointed out that the interstitial in silicon is still undetected. However, it is unreasonable to expect that they do not form as the damage event produces Frankel pairs i.e., interstitials and vacancies in equal numbers.* There have been several suggestions that the vacancies cluster to form higher order defects (Chadderton and Eisen, 1971; Brack et al., 1973). However, if this is the case, some vacnacy type defects ought to be observed.

The contrary is suggested by the present electron microscope studies. The defects formed on the annealing of iron implantation damage are <u>all</u> interstitial type (Chapter IV). This is also the result obtained by other workers using different implanted ions including P^+, B^+ and As^+ (Jenkins et al., 1973);

Another problem arises when the number of point defects involved in the damage process is considered. Some relevant numbers are given below for a typical 100 keV implant:

number of atoms displaced per incident P^+ ion:	1000
average number of point defects per cm^{-3} upon bombardment:	10^{22} (Ernisse, 1972)

---

*In addition to the atoms implanted which comprise under 0.1% of the defects produced.

number of Frank loops per cm^{-3} upon annealing:	10^{13}-10^{15}	(Davidson 1970 Madden 1973)
number of atoms in loops of size 300Å:	10^{3}	
loops per cm^{-3}:	10^{16}-10^{17}	
number of P^{+} ions implanted per cm^{-2} and cm^{-3}:	2×10^{14} cm^{-2} or 2×10^{18} cm^{-3}	

If 10^{22} Frenkel pairs form and subsequently annihilate, an excess of 10^{16}-10^{18} interstitials per cm^{-3} from which the loops are formed have to be accounted for.

It is significent that this is a small fraction (10^{-5}) of the Frenkel pairs originally produced and is of the same order as the number of dopant atoms implanted.

Clearly a model for the annealing process is required. The model ought to explain the presence of the interstitial defects as well as account for the annealing of divacancies in the 600°C range. It should assume that Frenkel pairs are produced by ion damage.

5.2. Model

Stage I Room temperature As implanted

In order to develop a model for the annealing process it is necessary to know the formation and migration energies of the point defects involved. In Table 5.1 the relevant information is listed. From this it is evident that at this stage (Stage I) the elementary interstitials and vacancies are mobile. In this model it is proposed that the interstitials travel away from the damaged zone and form submicroscopic clusters in the surrounding crystal. The compressive stress experienced within the damage zones due to their expansion (Tu et al., 1972) is of the order of 10^{19} dynes/cm^2 (Ernisse , 1971). This compressive stress promotes the drift of interstitials away from the amorphous zones into the less damaged regions the slower moving vacancies either annihilate interstitials or complex with each other to form divacancy and vacancy dopant complexes. The result would be a central damaged region rich in vacancies as proposed for metals (Nelson, 1969). Room temperature EPR evinces a high concentration (5 per ion) of divacancies in the heavily damaged crystal as shown in Fig. 5.1 (Vook and Stein, 1969; Daley, 1969). A large fraction of the 10^{22} Frenkel pairs per cm^3 (1000 per ion) annihilate. As suggested by the investigators the measured divacancy concentration of five per ion is probably an underestimate because their method does not detect those vacancies incorporated in the core itself. Supposing as many as half the Frenkel pairs annihilate by direct recombination of vacancies and interstitials about 10^{20}-10^{19} vacancies and interstitials will remain at this stage. Interstitials which have formed small stable

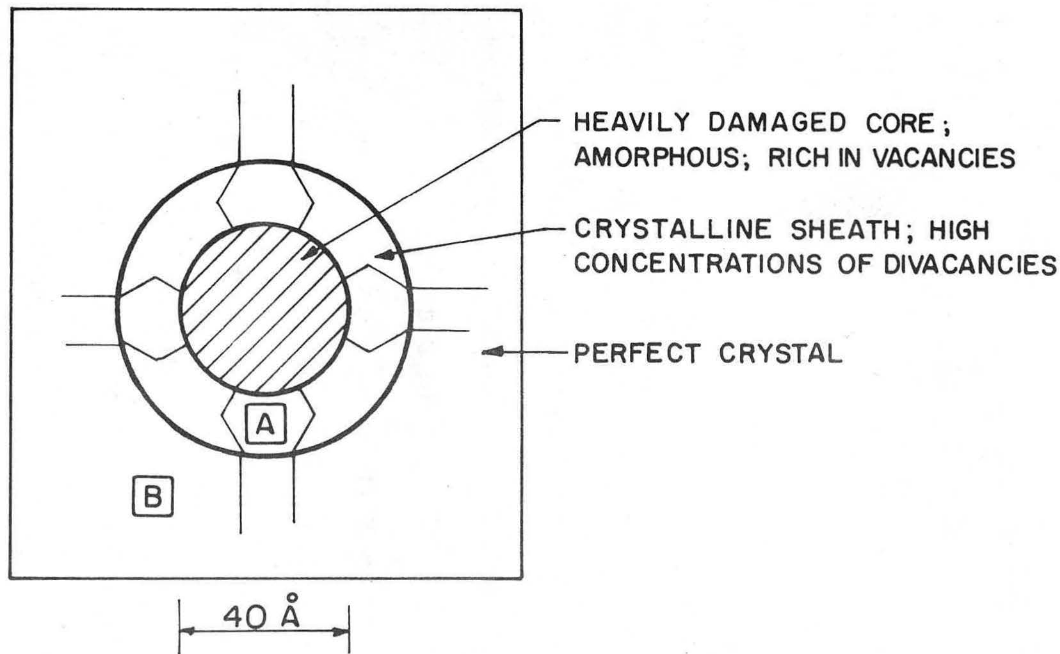

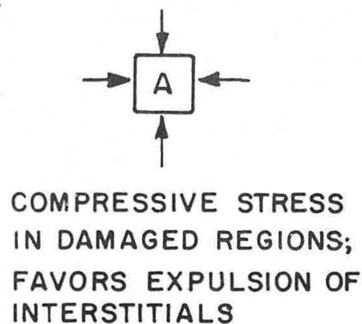

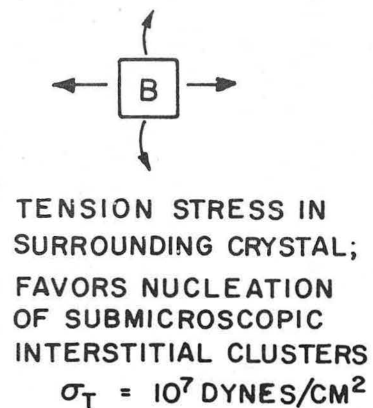

XBL 7412-7632

Fig. 5.1. Shows a model of a damage duster formed at the end of an ion track. Interstitials are expelled from the regions in compression A to those in tension B where they may cluster.

clusters probably also incorporate those dopant atoms not already complexed with vacancies.

Other workers have suggested the existance of submicroscopic clusters. Based on X-ray lattice parameter data clusters of interstitials and vacancies have been suggested in neutron irradiated silicon (Baldwin, 1965). More recently low temperature photoluminescence investigations of ion implanted silicon have shown evidence of interstitial clusters. However, the constituants of the clusters were not determined (Noonan et al., 1974).

Stage II 300-600°C

EPR evidence shows that this region corresponds to first the formation of numerous divacancies and at higher temperatures to their annealing out. In this model the central damaged regions are expected to repair by the emission of vacancies some of which form divacancies in the lower temperature ranges 300-400°C. At higher temperatures 400-600° the divacancies (see Table 5.1) become mobile and annihilate the interstitial clusters and complex with the dopant atoms.

Electron diffraction patterns of thin foils in the as received condition and after annealing to 400°C are shown in Fig. 5.2a,b respectively. The faint rings in Fig. 5.2a indicate the presence of a high density of amorphous zones (the spots appear from the crystalline substrate). The rings disappear when the substrate is heated to 400°C (Fig. 5.2b). This is an agreement with EPR data that isolated amorphous zones anneal at 400°C.

The diffraction pattern in Fig. 5.2b shows pronounced streaking in the 111 directions as well as a set of 111 reflections. Figure 5.3

shows how the streaks and spots can be correctly accounted for if each 220 reflection in the zero Laue layer (Fig. 5.3 at B) and each 111 reflection in the first Laue layer (Fig. 5.3 at A) is extended in the four 111 directions.

(This is further illustrated in Fig. 5.4 which shows the zero and the first Laue layer in various projections. A "possible" shape of the cluster which could give rise to such extensions in reciprocal space is shown in Fig. 5.4c). A dark field image of the streaks (Fig. 5.5) shows small granular areas 50-70Å wide. The streaks could then be interpreted as the rel-rods or planes in reciprocal lattice produced by small clusters on the four {111} planes. The granular areas in Fig. 5.3 are evidently diffraction contrast produced by the clusters.

A possible alternative suggestion from a study of heavily damaged substrates (Matthews, 1971) is that the 111 streaks arise from high densities of "microtwins and faults". Upon annealing, such foils yield a complex defect structure of dislocation networks (Tamura, 1972; Madden, 1973). However, the substrates used in this study were damaged to below the critical dose where a continuous amorphous layer is not formed. Further the defects formed upon the annealing of damage are interstitial Frank loops. It is not possible to explain how "micro twins and faults" could age to produce a family of Frank loops. It is, therefore, reasonable to interpret the streaking as arising from small clusters on the close packed planes which, at higher annealing temperatures, combine to form Frank loops.

It was not possible to determine the nature of these clusters that gave rise to rel rods in the early stages of annealing. Both interstitial and vacancy type could be present, about 10^{17}-10^{19} defects 1 cm^3.

If small interstitial clusters do exist at 600°C it provides a possible explanation for the inactive dopants. According to EPR data most of the vacancy dopant complexes anneal out at this temperature. However, electrical measurements show only 50% dopant activity is achieved. It is proposed that the inactive dopant atoms are still complexed with the interstitial clusters at this stage.

Stabe III 600-800°C

In the early stages the break up of small interstitial clusters proceeds with the absorbed dopant atoms becoming substitutional. Most of the interstitials annihilate the remaining vacancy clusters. At the same time a few of the clusters, interstitial and vacancy, convert to Frank loops on the close packed planes.

At this stage two effects which result in the formation of large interstitial loops and rod defects become significant. The first is the slightly higher strain interaction between the interstitial and the dislocation lines as compound to that between a vacancy and the dislocation line. Consequently, dislocation loops will tend to trap a few more interstitials than vacancies. This will tend to cause the vacancy loops to shrink and the interstitial loops to grow.

This effect alone might account for the predominance of interstitial loops, after high temperature annealing; the excess vacancies would be assumed to have reached the surface.

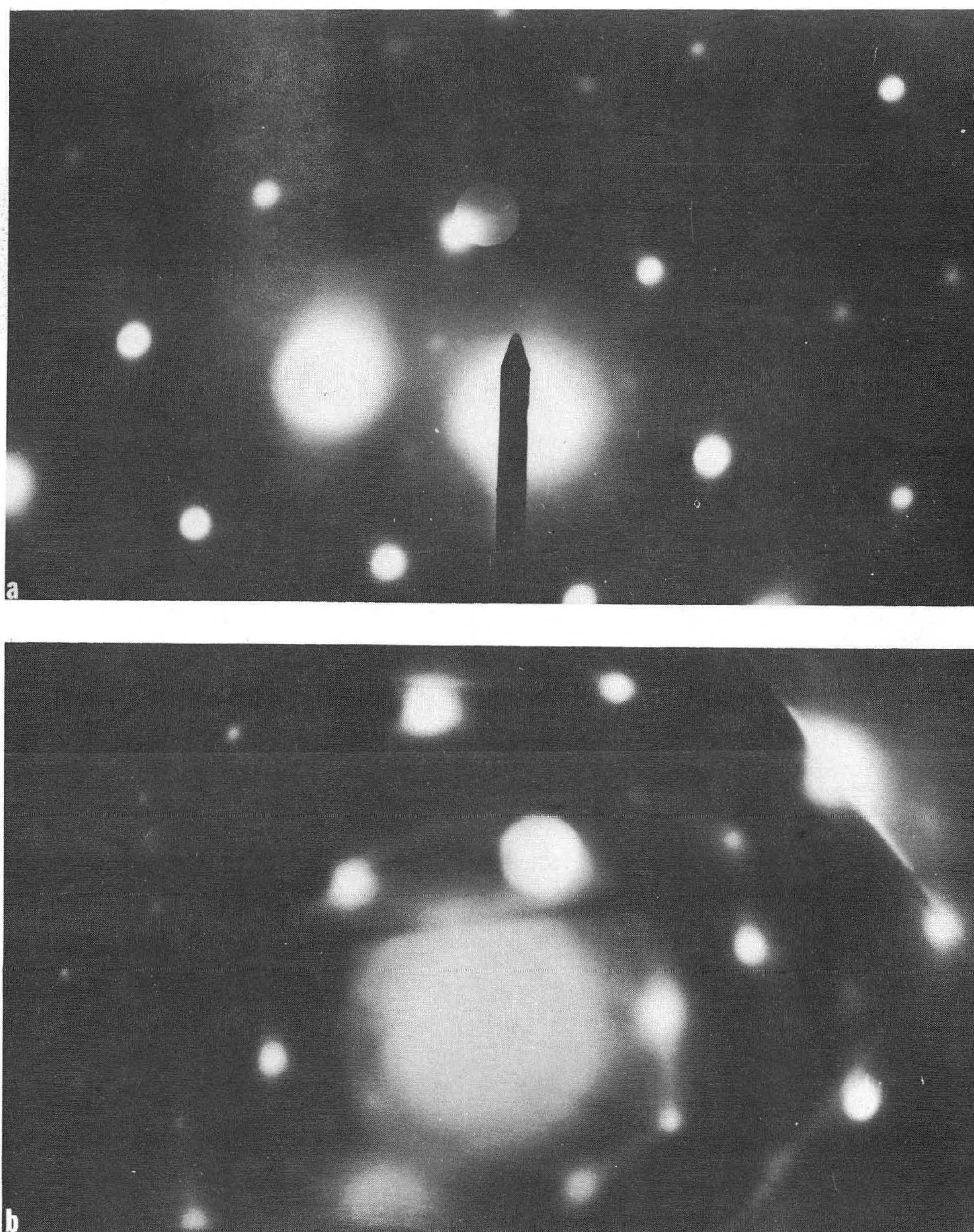

XBB 7411-7728

Fig. 5.2. Diffraction patterns from (a) and as received sample (b) a sample annealed at 400°C for 15 min. In the as received samples faint rings from the amorphous layers were observed. Upon annealing (b) these faint rings disappear and well developed streaking in the ⟨111⟩ directions and a set of ⟨111⟩ spots were observed.

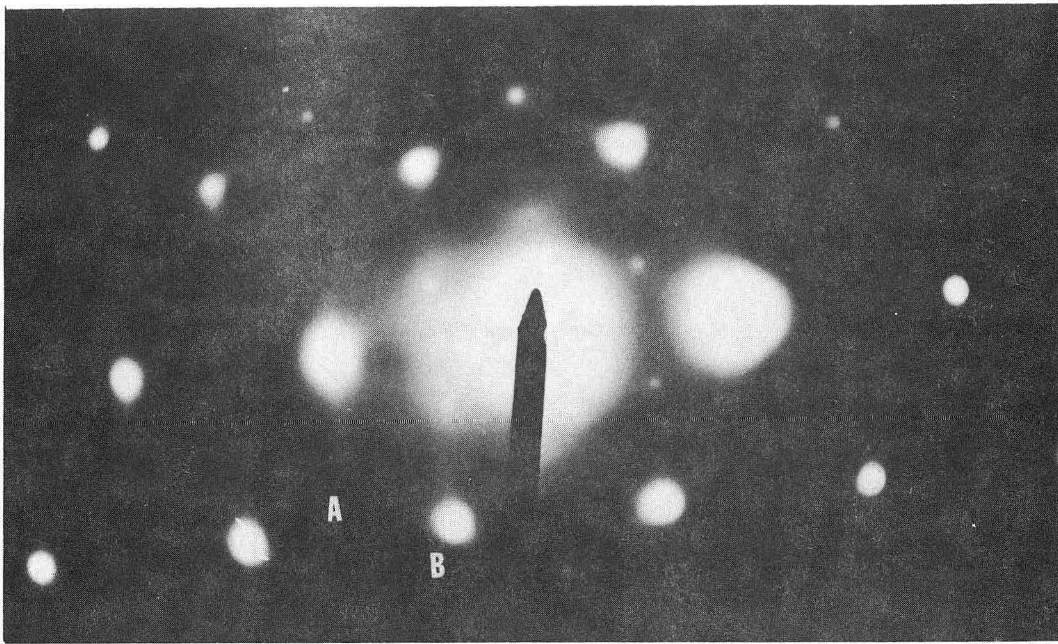

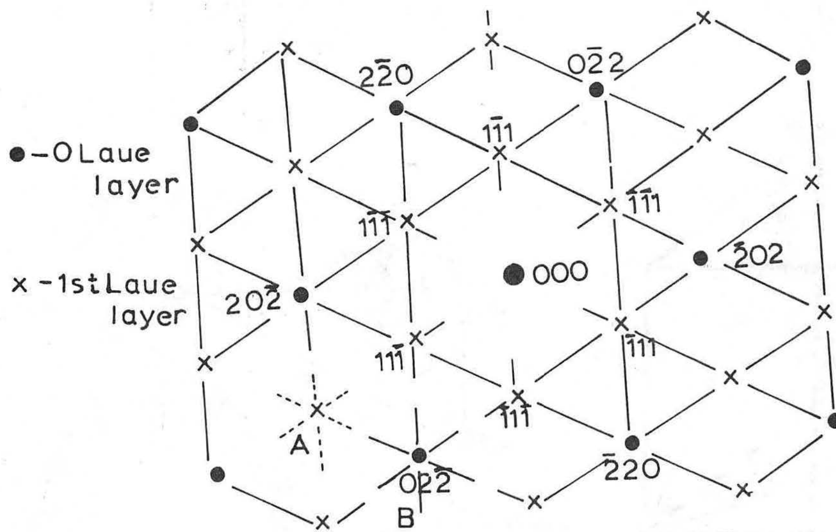

XBB 754-3248

Fig. 5.3. Shows how the streaks and the extra spots can all be accounted for by assuming that the {111} spots of the first Laue layer A and the 220 spots of zero Laue layer B are extended in the fair ⟨111⟩ directions.

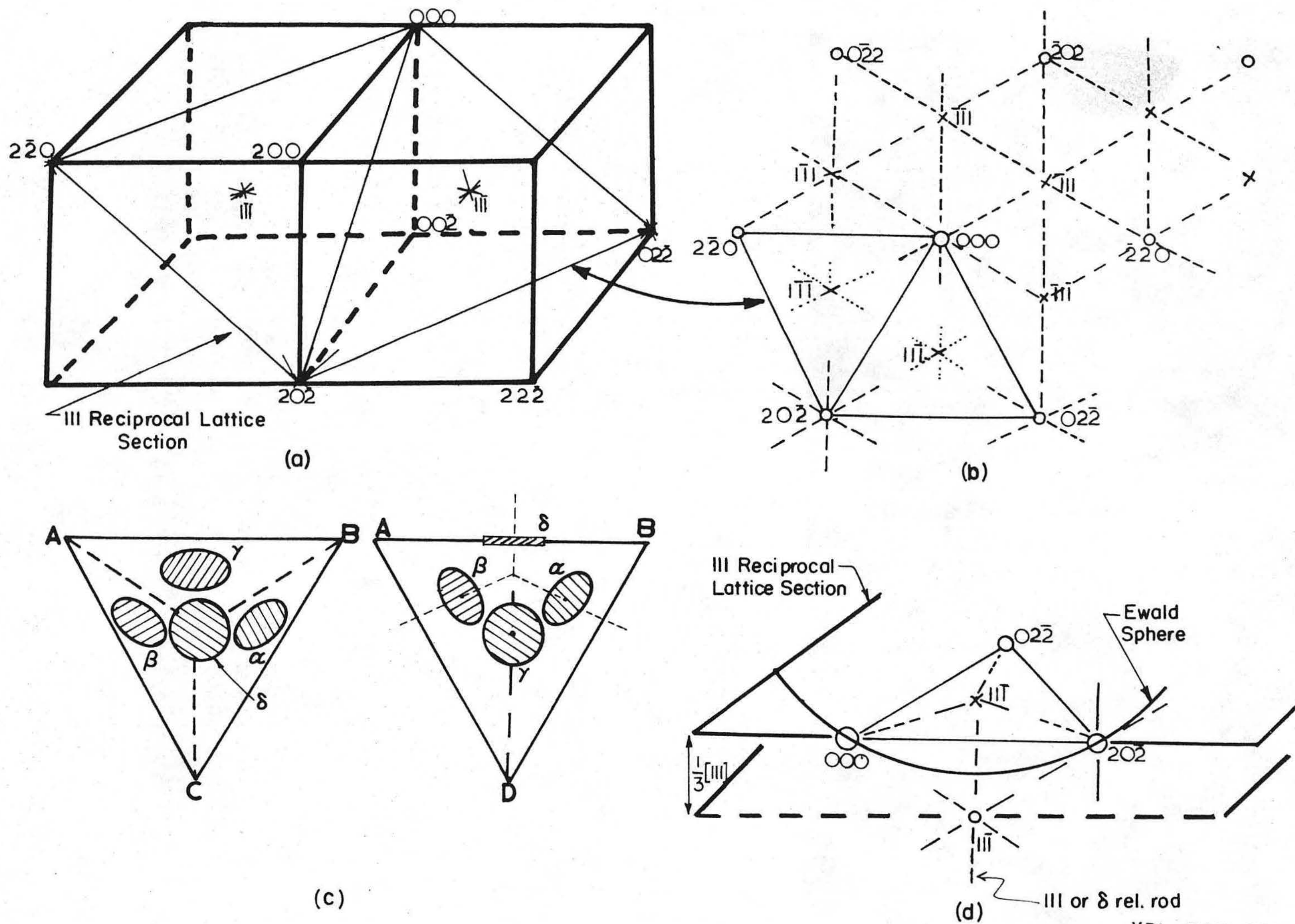

XBL 747-6779

Fig. 5.4. (a) Shows the reciprocal lattice section of a fcc cell with the zero and the first Laue layer. (b) Shows the projection of (a) in the ⟨111⟩ direction. (c) Shows a "possible" cluster that could give rise to such streaks.

XBB 747-4767

Fig. 5.5. Dark field image of the streaks showing the defect clusters that give rise to the streaking. It is argued (see text) that these could be small clusters of point defects which upon annealing at 800°C give rise to Frank loops.

However, the predominance of interstitial loops in these foils can also be explained in another way. It is assumed that when isolated amorphous zones are found increase in the total number of lattice sites due to recrystallization of these zones. This is reasonable as long as a continuous amorphous layer has not been formed. Then as the dopant atoms become substitutional by combining with a various an equivalent number of silicon atoms must remain interstitial. Therefore, when all of the vacancy defects have been annihilated by recombining with interstitials there will still be some interstitials left. These would be just enough to account for the growth of the observed interstitial defects by conversion of a few of the original small interstitial clusters into frank loops.

In the 800°C range the well developed Frank loops with their enclosed stacking faults can still provide special sites for the remaining invactive dopants. The total number of interstitials involved in the secondary defects is always less than the atoms displaced when the implanted dopant atoms become substitutional. This is in agreement with calculations performed in Boron implanted foils (Bicknell, 1969) where it was shown that the number of atoms in the loops equals roughly the number of dopants implanted.

Stage IV 800-900°C

This corresponds to the highest temperature ranges where the loops shrink under their own line tension. Seegar (1970) has proposed that at this temperature an interstitial diffusion mechanism operates. Vacancies could also be nucleated at the surface and migrate to the loops.

In this temperature range, 100% electrical activity is finally attained. This is explained on the basis that when the loops shrink the dopant atoms within the stacking fault and dislocation cores finally come to occupy regular substitutional sites. A summary of the four stages is given in Table 5.2.

Table 5.1.
Formation and migration energy of point defects in silicon.

		Author	eV	Temperature at which Defects Anneal
E_V^F	Energy of formation of a vacancy	Benneman (1965) Seeger-Chick (1968) Seegar (1971) Swalin (1972)	2.13 2.97 4.63* 2.0	
E_V^M	Energy of migration of vacancy	Watkins (1965) Wahn (1965)	0.33 Voneutral 0.15 V found in n-type Si 0.16	~300°K 70-85°K
E_{V-V}^F	Energy of formation of a divacancy	Seeger & Chick (1968)	4.66	
E_{V-V}^M	Energy of migration of divacancy	Stein (1971)	1.3 0.4 V-V = 0.25 V-V =	600-700°K 550°K
E_{V-V}^B	Binding energy of divacancy	Seeger & Chick (1968)	1.27	
E_I^F	Energy of formation of interstitial	Benneman (1965)	1.09	

Table 5.1. Continued.

		Author	eV	Temperature at which Defects Anneal
E_I^M	Energy of Migration of an Interstitial	Seegar (1971)	0.85	Room Temperature
		Benneman (1975)	0.51	
		Hasiguti (1966)	<0.22	
		Watkins (1965)	~0 p-type	~4.2°K
			~0.4 n-type	~170°K

*Calculated

K. H. Benneman, Phys. Rev. 130, 1763 (1963).
R. R. Hagiguti, J. Phys. Soc. Japan 21, 1927 (1966).
A. Seeger and K. P. Chik, Phys. Stat. Sol. 29, 455 (1968).
A. Scholz-A. Seeger, Phys. Stat. Sol. 3, 1480 (1963).
A. Seeger, Rad. Eff. 9, 15 (1971).
H. J. Stein, Rad. Eff. 9, 195 (1971).
R. A. Swalin, Thermodynamics of Solids (J. Wiley, N. Y., 1972), p. 299.
R. E. Wahn, Phys. Rev. 140, A690 (1965).
G. D. Watkins, Radiation Damage in Semiconductors (Dunod Paris, 1965), p. 97.

Table 5.2. Summary of the four stage process leading to interstitial defects in ion implanted silicon.

Stage	Interstitial	Vacancies	Temp.
I	Interstitials mobile during implant. Annihilate vacancies. Form interstitial clusters. Affected by stresses in damaged layer. $10^{22}/cm^3$ defects formed. $\sim10^{19}/cm^3$ defects in clusters.	Form divacancies annihilated. Form V-P, V-O complexes.	Room Temp. to 300°C
II	Interstitial clusters stable; some break up and are annihilated. Association of dopants with the interstitial clusters. $\sim10^{17}$ defects/cm^3	Break up of V-V, V-P, V-Sb complexes. Migration and annihilation of vacancies. Divacancy annealing (escape of excess vacancies).	300°C-500°C
III	Break up of interstitial clusters. Conversion of interstitial clusters to dislocation loops. Segregation of dopants atoms $\sim10^{15}$ defects/cm^3	Formation of vacancy loops. Dislocation attract interstitials and vacnacy loops shrink.	500°C-700°C
IV	Well developed interstitial loops--hexagonal in stage, ~300Å; 10^{15} defects/cm^3 involving about 10^{15} atoms/cm^3. Total number of ions implanted = $2\times10^{18}/cm^3$	Vacancy loops all annihilated.	~800°C

5.3. Applications of the Model

The model proposed above has two simple consequences which explain the experimental results of other workers. First, in the case where the damage layer is continuous a complex structure of dislocation networks develop suggesting that the damaged layer anneals by epitaxial growth from small remaining islands of crystal. In such cases, for phosphorous, complete electrical activity of the dopant is achieved after a mild anneal of 600°C (Gibbons, 1972; Crowder and Morehead, 1969).

In terms of the present model the continuous amorphous layer relaxes the assumption that the volume of the crystal must remain unchanged. Consequently, the host interstitial atoms and the implanted dopant atoms can all find substitutional sites; additional atom layers can be formed during regrowth of the continuous amorphous layer. The observed dislocation tangles (Tamura et al., 1972) are consistent with this idea. The achievement of electrical activity is associated with the dopant becoming substitutional on a regular lattice site. Apparently, rather few phosphorous dopant atoms are attracted to the dislocation cores (Gibbons, 1969).

The second consequence of the model is the explanation of the contrast effects seen in Chapter IV. An example of this for loops in the foil plane is seen in Figs. 4.8 and 4.9. In Fig. 4.8 and Fig. 4.9 the effect of changing g from +111 to -111 is shown. Notice how the loops appear dark in the inside image (4.8b) and faint in Fig. 4.8c. A similar effect is seen in weak-beam conditions Fig. 4.9.

This may be a structure factor contrast arising from the dopant atoms being attracted to the stacking faults associated with the

loops. The similar effect observed in the perfect loop images first seen by Davidson and Booker (1970) might also be explained if some excess dopant concentration remains after unfaulting. The effect of this segregation on the displacement vector of the fault and on diffraction contrast is discussed below.

In Fig. 5.7, the $(1\bar{1}0)$ projection of a diamond cubic cell (Hornstra, 1968) is shown. The distance between the a layer and A layer is a/12[111]. An extrinsic fault is then made by inserting a double layer A-a into the perfect crystal. This is shown in Fig. 5.3. The vector is then a/3[111]. Atoms whose sizes are close to that of silicon e.g., phosphorous could be incorporated in the stacking fault possibly complexed with vacancies. Such atoms are only weakly attracted to the dislocation core (Gibbons, 1972). However, the ⟨111⟩ direction in which the dotted bonds extended are expected to be soft and change to accommodate the absorbed atom (Fig. 5.3). The percentage of such atoms are expected to be 10-15%. Since phosphorous is smaller than silicon the c layer is expected to move slightly closer to a. The Burgers vector is no longer a/3[111] but a/3[111]--p·a/12[111]. If p = 1, b = a/4[111]. Thus for small amounts of phosphorous p is expected to be in the range $0 < p < 1$. The Burgers vector of a Frank loop with segregation may then be written as a/3[111] - a/g[111] or a/x[111] with x greater than three. The phosphorous atoms thus adsorbed may be electrically inactive as they are in a region of different crystal structure and may not provide the same electronic energy levels as they do in a regular site. Recently, Lee et al. (1973) observed a special spectrum in neutron irradiated silicon which he attributed to a possible phosphorous vacancy complex. The

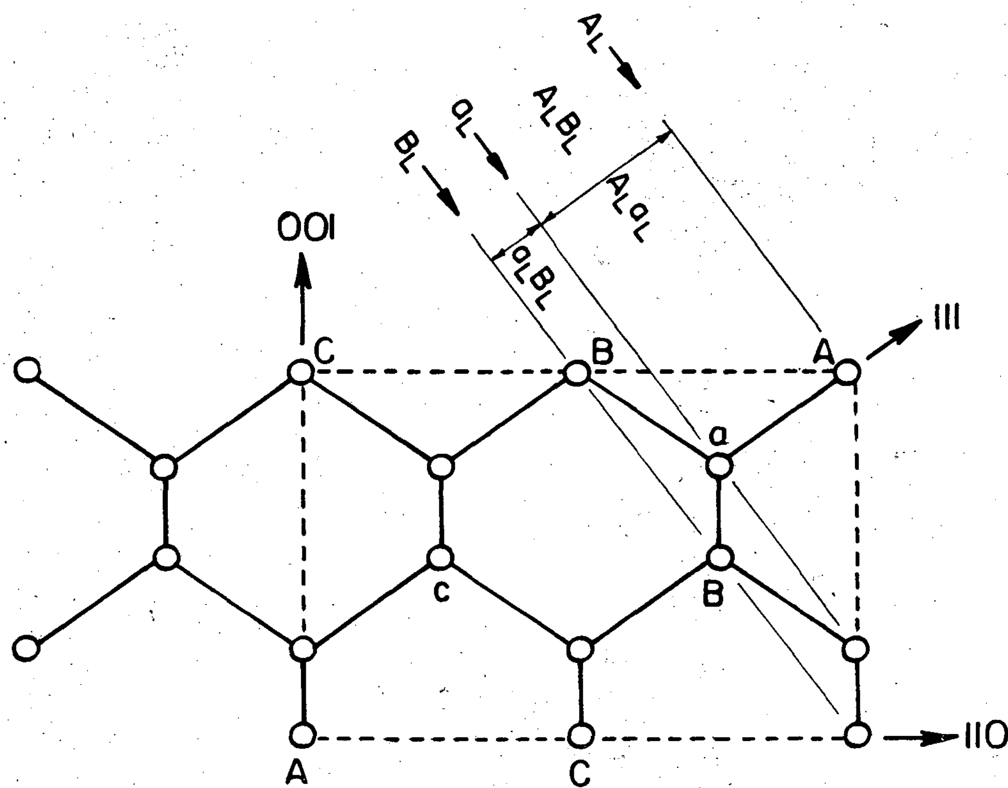

$$A_L B_L = \frac{a_o}{3}[111]$$

$$AB = \frac{a_o}{\sqrt{2}} \text{ along } [110]$$

since $a_L B_L = A_L B_L - A_L a_L$

and $\underline{A_L a_L} = \frac{AB}{2} \Big/ \cos\langle 110/111 \rangle$

$$= \frac{a_o}{2\sqrt{2}} \, \frac{\sqrt{3}}{\sqrt{2}} = \frac{a_o}{4}[111]$$

$$\therefore \quad aB_L = \frac{a_o}{3}[111] - \frac{a_o}{4}[111]$$

i.e. $\underline{aB_L} = \frac{a_o}{12}[111]$

XBL 747-6680

Fig. 5.6. The $(1\bar{1}0)$ projection of a diamond cubic cell (after Hornstra, 1968). The distance between the a and B layer, aB_L, is shown to be $a_o/12[111]$.

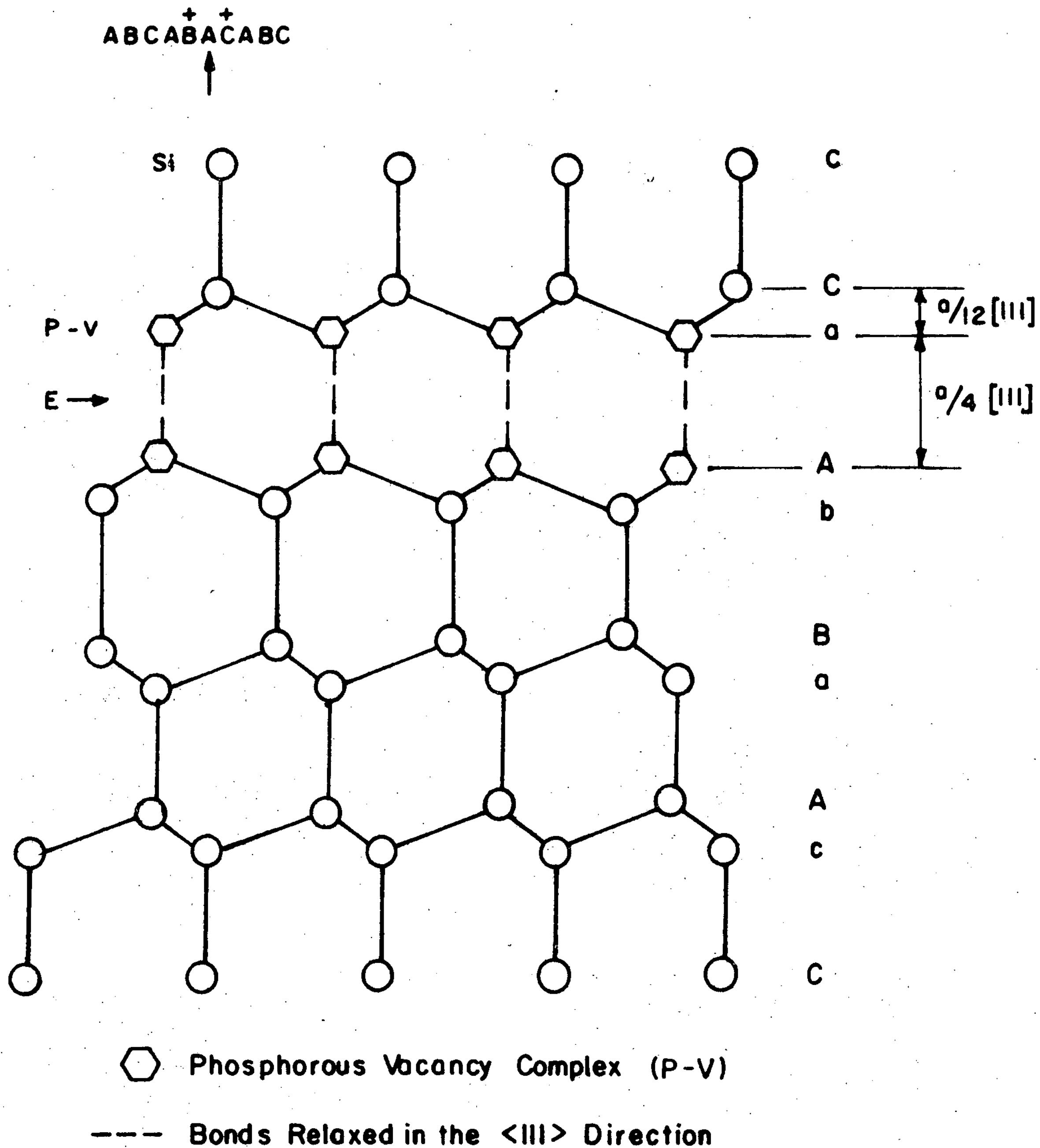

Fig. 5.7. An interstitial fault (E) caused by the insertion of an extra A-a layer. The dotted bonds in the (111) direction are "soft" and could accommodate a phosphorous-vacancy complex instead of a silicon atom. This would result in a small change of the fault vector from a/3[111] to a/x[111], x>3.

defect has an extra localized electron and the phosphorous atom is compensated.

In terms of the model presented in this chapter, this p-vacancy complex could segregate to the hexagonal atom positions on the fault as shown in Fig. 5.3. The consequent relaxation of the bonds in the [111] direction yields a fault vector of a/x[111] with $x > 3$ as explained previously.

The contrast feature in the Frank loops shown in Figs. 4.8 and 4.9 is explicable in terms of the dopants segregating on the stacking fault. The contrast effect in the prefect loops is explicable on the basis of the dopant vacancy complexes remaining after the Frank loops have unfaulted. This reaction is expected to proceed as

$$a/3[111] = a/y[111] + a/6[11\bar{2}] = a/2[110] - a/y[111] \quad .$$

The perfect loops then have a small displacement "fault" of a/y[111]. Such a displacement acts effectively as a structure factor contrast would arise.

5.4. Conclusions

A model that explains the annealing process of ion implantation damage in silicon and the presence of the experimentally observed interstitial defects has been developed. It is suggested that submicroscopic interstitial clusters form for the case of subcritical damage. These occur in addition to vacancy clusters consistent with the fact that Frankel pairs are produced by the bombarding ions. A four stage process is developed with accounts for the presently known behavior of vacancies. Two effects are used to develop the model. The first is the slightly greater interaction between the interstitial and the dislocation line than that between the vacancy and the dislocation. This increases the chances of survival of interstitial loops over vacancy loops. The second is that discontinuous damage does introduce any lattice sites even when it recrystallizes. Therefore, the implanted dopants displace 10^{18} atoms/cm^3 during annealing which can account for the interstitial defects.

The poor electrical activity of the P^+ ions in the 2×10^{14} range (discontinuous damage range) which cannot be explained on the basis of their interaction with the dislocation core is explained on the basis of their interaction which the stacking fault within the Frank loops. This segregation also may explain the anomalous contrast effects observed in the electron microscope images of these and perfect loops.

"Between you and them is distance
Uncertainty--
Care".

D. J. Hammarsjkold

ACKNOWLEDGEMENTS

Not merely more metallurgy but an attitude to life and thought I have learned from Professor Washburn's discerning guidance. Any competence the electron microscopy may show is probably traceable to Professor G. Thomas and his unflagging goading to try new methods. To many I owe thanks for giving me their help and sharing with me their humanity--to many to name individually--those not to be omitted are the Merriams, the Howitts, Margaret Robson and Thorvald Astrup. To Patti Fenton I owe instructive distraction and the human lesson. We thank Dr. V. G. K. Reddi of Fairchild R & D Division, Palo Alto, CA for kindly supplying the ion-implanted samples. My thanks to Jean Wolslegel for the patient typing and to the Energy Research and Development Administration for financial support.

REFERENCES

T. O. Baldwin, The Effects of Fast Neutron Irradiation at Ambient Temperature on the Lattice Parameter of Silicon and Germanium. Phys. Rev. 21, 901 (1968).

W. L. Bell and G. Thomas, Useful Properties of Dark Field Images. Phys. Stat. Sol. 12, 843 (1965).

R. W. Bicknell, The Distribution of Condensed Defect Structures Formed in Annealing Boron-implanted Silicon. Proc. Roy. Soc. (London) 311A, 75 (1969).

R. W. Bicknell, Weak-beam Observation of Dislocation Loops in Silicon J. Microscopy 98, 165 (1973).

R. W. Bicknell,, R. M. Allen, Correlation of Electron Microscope Studies with the Electrical Properties of Boron Implanted Silicon, Radiation Effects, 6, 45 (1970).

L. T. Chadderton and F. H. Eisen, On Annealing of Damage Produced by B^+ Ion Implantation in Silicon Single Crystals, Radiation Effects 7, 129 (1971).

L. J. Chen, K. Seshan, G. Thomas, Contrast and Resolution of Small Dislocation Loops in HVEM, Phys. Stat. Sol. (to be published, 1975).

L. J. Chen, Theoretical and Experimental Analysis of Crystal Defects with Particular Emphasis to Silicon (Ph. D. Thesis), LBL-3179, May, 1974.

L. J. Cheng, T. C. Corelli, J. W. Corbett and G. D. Watkins, 1.8-, 3.3-, 3.9μ Bands in Irradiated Silicon: Correlations with the Divacancy. Phys. Rev. 152(2), 761 (1966).

B. L. Crowder, Private Communication, 1974.

B. L. Crowder, F. F. Morehead, Jr., Annealing Charateristics of n-type Dopants in Ion-Implanted Silicon. Applied Phys. Letters 14:10 313 (1969).

B. L. Crowder and R. S. Title, The Distribution of Damage Produced by Ion-Implantation of Silicon at Room Temperature. Radiation Effects 6, 63 (1970).

D. J. H. Cockayne, I. L. F. Ray and M. J. Whelan, Investigation of Dislocation Strain Fields Using Weak Beams. Philosophical Magazine 20, 1265 (1969).

D. F. Daley and K. A. Pickar,EPR in Ion Implanted Silicon, Appl. Phys. Lett. 15, 267 (1969).

S. M. Davidson and G. R. Booker, Damage Produced by Ion Implantation in Silicon, Radia. Eff. 6, 45 (1970).

J. W. Edington and R. E. Smallman, Faulted Dislocation Loops in Quenched Aluminium, Philosophical Magazine 11, 1109 (1965).

E. P. Ernisse, Sensitive Techniques for Studying Ion-Implantation Damage, Applied Physics Letters 18, 581 (1971).

J. F. Gibbons, Ion-Implantations in Semiconductors, Pt. I, Proceedings IEEE 56, 3, 295 (1968).

J. F. Gibbons, ibid, Part II. Proceeding IEEE 60 (9), 1067 (1972).

J. F. Gibbons, On the Effectiveness of Dislocation Loops for the Adsorption of Implanted Ions, Radiation Effects 6, 313 (1970).

W. M. Gibson, F. W. Martin, R. Stensgaard, F. Plamgren Jensen, N. I. Meyer, G. Galster, A. Johnsen and J. S. Olsen, Electrical and Physical Measurements on Silicon Implanted with Channeled and

Non-Channeled Dopant Ions, Canadian J. Phys. 46, 675 (1968).

P. B. Hirsch, A. Howie, R. B. Nicholson, D. W. Pashley, M. J. Whelan, Electron Microscopy of Thin Crystals (Butterworths, 1965a), p. 205.

J. P. Hirth and J. Lothe, Theory of Dislocations (McGraw Hill, Inc., 1968).

J. Hornstra, Dislocations in the Diamond Lattice, J. Phys. Chem. Sol. 5, 129 (1958).

A. Howie, Z. S. Basinski, Approximations of the Dynomicel Theory of Diffraction Contrast, Philosophical Magazine 17, 1039 (1968).

C. J. Humphreys, The Optimum Voltage in Very High Voltage Electron Microscopy, Philosophical Magazine 25, 1459 (1972).

C. J. Humphreys, L. E. Thomas, J. S. Lally, R. M. Fisher, Maximizing the Penetration in High Voltage Electron Microscopy, Philosophical Magazine , 87 (1971).

M. L. Jenkins, D. J. H. Cockayne and M. J. Whelan, The Geometry of Small Frank Loops, J. Microscopy 98, 155 (1973).

P. M. Kelley and R. H. Blake, The Symmetric Weak Beam Method and Its Application to Dislocation Loop Analysis, Philosophical Magazine 28, 475 (1973).

Y. H. Lee, Y. M. Kim, J. W. Corbett, New EPR Spectra in Irradiated Silicon, Radiation Effects 15, 78 (1972).

P. K. Madden, Structural and Electrical Studies of Ion-Implanted Semiconductors (Ph. D. Thesis), University of Oxford (1974).

M. D. Mathews, Electrical and Electron Microscopy Observations on Dejects in Ion-implanted Silicon, Rad. Eff. 11:3-4 , 167 (1971).

J. W. Mayer, Ion Implantation Semi-conductors: Lattice Disorder and Electrical Effects, IEEE Trans. 15(6), 10 1968).

J. W. Mayer, Ion Implantation - Lattice Disorder, Radia. Eff. 8, 269, (1971).

D. Mazey, R. J. Nelson and A. S. Barnes, Observation of Ion-bombardment Damage on Silicon, Philosophical Magazine 17, 1145 (1968).

F. F. Morehead, Jr. and B. L. Crowder, A Model for the Formation of Amorphous Si by Ion-bombardment, Radia. Eff. 6, 27 (1970).

R. S. Nelson, The Physical State of Ion-implanted Solids, Proc. Roy. Soc. A311, 53 (1969).

J. R. Noonan, C. A. Kirkpatrick and B. G. Streetman, Low Temperature Photoluminescena from Boron Ion-implanted Silicon, Radia. Eff. 21, 225 (1974).

R. Osiecki and G. Thomas, Enhanced Resolution of Dislocation Imaging at High Voltages, Proc. 29th Annual Conference, Baton Rouge, LA, (1971), p. 178.

J. R. Parsons, Conversion of Crystalline Germanium to Amorphous Germanium by Ion-Bombardment, Philosophical Magazine 12, 1159 (1965).

R. C. Perrin and B. L. Eyre, The Application of Weak Beam Imaging to Studies of Small Dislocation Loops, J. Microscopy 98(2), 200 (1973).

A. Seeger, Investigation of Point Defects in Silicon and Germanium by Non-irradiation Techniques, Radia. Eff. 9, 15 (1971).

A. Seeger and K. P. Chik, Diffusion Mechanisms and Point Defects in Silicon and Germanium, Phys. Stat. Sol. 29, 455 (1968).

K. Seshan and J. Washburn, On the Precipitation of Phosphorous in Ion-Implanted Silicon, Radia. Eff. 14, 271 (1972).

K. Seshan, Non-Conventional Electron Microscopy in Small Defect Characterization, Proceedings 32nd Annual EMSA Meeting, Claitor Publishers, Baton Rouge, LA, 1974.

K. Seshan and J. Washburn, Some New Results in the Characterization of Defects in Ion-implanted Silicon, Radia. Eff. (1975).

H. J. Stein, Depth in Silicon, Concepts and Correlation, Radiation Effects 9, 175 (1971).

H. J. Stein, F. L. Vook and J. A. Borders, Direct Evidence of Divacancy Formation in Silicon by Ion-implantation, Appl. Phys. Lett. 14, 328 (1969).

G. D. Watkins, Radiation Damage in Semiconductors (Donod de Paris, 1965), p. 97.

W. K. Wu, J. Washburn, Identification of Interstitial and Vacancy Type Dislocation Loops in Ion-implanted Silicon, J. Appl. Phys. 45, 1085 (1974).

LEGAL NOTICE

This report was prepared as an account of work sponsored by the United States Government. Neither the United States nor the United States Energy Research and Development Administration, nor any of their employees, nor any of their contractors, subcontractors, or their employees, makes any warranty, express or implied, or assumes any legal liability or responsibility for the accuracy, completeness or usefulness of any information, apparatus, product or process disclosed, or represents that its use would not infringe privately owned rights.

TECHNICAL INFORMATION DIVISION
LAWRENCE BERKELEY LABORATORY
UNIVERSITY OF CALIFORNIA
BERKELEY, CALIFORNIA 94720